Transport in Spinless Superconducting Wires

Junaid Majeed & Abhishek Dhar

International Centre for Theoretical Sciences, Bengaluru-560089

ICTS | INTERNATIONAL CENTRE for THEORETICAL SCIENCES

TATA INSTITUTE OF FUNDAMENTAL RESEARCH

Introduction

The Kitaev chain models a one-dimensional spinless p-wave superconductor [1] and provides one of the simplest examples of a topological insulator. This system has the so-called Majorana Bound States (MBS), which are topologically protected zero-energy bound states, localised at the boundaries of an open chain. Several proposals were put forward [2] to realise the Kitaev chain experimentally and observe the MBS. Some of these experimental proposals have already been successfully implemented [3, 4]. One of the key experimental signatures of the MBS is the zero-bias peak in the differential tunnelling conductance and Ref. [3, 4] were some of first experiments which reported evidence for this peak. More interesting topological phases are revealed as one goes beyond the nearest neighbour Hamiltonian in a Kitaev chain. In particular, Ref. [5] shows the existence of two different topologically non-trivial phases in a 1-D Kitaev chain with next to nearest neighbour couplings.

We consider a superconducting wire connected to two reservoirs kept at temperatures T_L and T_R respectively and use the QLE-NEGF approach to obtain the exact steady state properties e.g. particle and heat current and conductance etc. These quantities are obtained in terms of multiple NEGF transmission coefficients, which could be interpreted physically as well. This approach has been used in Ref. [6] to study conductance of a one-dimensional system consisting of a p-wave superconductor connected to leads at the two ends (NSN junction).

Methods

- We take the Hamiltonian of the full system of wire and baths as follows:

$$\mathcal{H} = \mathcal{H}^W + \mathcal{H}^{WL} + \mathcal{H}^{WR} + \mathcal{H}^L + \mathcal{H}^R, \tag{1}$$

where

$$\mathcal{H}^W = \sum_{mn} H^W_{mn} c^\dagger_m c_n + \Delta_{mn} c^\dagger_m c^\dagger_n + \Delta^\dagger_{mn} c_m c_n, \tag{2}$$

$$\mathcal{H}^{WL} = \sum_{\nu m} V^L_{m\nu} c^\dagger_m c_\nu + c.c., \quad \mathcal{H}^{WR} = \sum_{\nu' m} V^R_{m\nu'} c^\dagger_m c_{\nu'} + c.c., \tag{3}$$

$$\mathcal{H}^L = \sum_{\mu\nu} H^L_{\mu\nu} c^\dagger_\mu c_\nu; \quad \mathcal{H}^R = \sum_{\mu'\nu'} H^R_{\mu'\nu'} c^\dagger_{\mu'} c_{\nu'}. \tag{4}$$

$\mathcal{H}^{L/R}$ are the Hamiltonians of the left/right reservior respectively, $H^{WL/R}$ model the coulplings of the wire with Hamiltonian, $\mathcal{H}^W$, with the two reserviors. The model considered here is quite general in the sense that we allow non-zero hopping elements between arbitrary sites and similarly the superconducting pairing term is allowed between any pair of sites. Thus there are no restrictions on dimensionality and the structure of the underlying lattice and the range of the interactions. The results for the one-dimensional Kitaev chain with nearest neighbor interactions follows as a special case.

- In the QLE-NEGF approach, the following steps are followed in general:

1. Write down the Hiesenberg equations of motion the wire and the reservoirs.
2. Obtain a formal solution for the reservoir equation of motion using the reservoir Green's functions. These for our case look like,

$$g^+_L(t) = -ie^{-itH^L}\theta(t) = \int_{-\infty}^{\infty} \frac{d\omega}{2\pi} g^+_L(\omega) e^{-i\omega t}, \quad g^+_R(t) = -ie^{-itH^R}\theta(t) = \int_{-\infty}^{\infty} \frac{d\omega}{2\pi} g^+_R(\omega) e^{-i\omega t}. \tag{5}$$

3. Use the formal solution to obtain the effective equation of motion for the wire operators. For this model we obtain this equation to be,

$$i\dot{c}_l = \sum_m H^W_{lm} c_m + \sum_m K_{lm} c^\dagger_m + \eta^L_l(t) + \eta^R_l(t) + \int_{-\infty}^{t} ds \left([\Sigma^+_L(t-s)]_{lm} + [\Sigma^+_R(t-s)]_{lm} \right) c_m(s).$$

Thus, the effect of the reservoirs on the dynamics of the wire operators is expressed as the sum of the noise $\eta^L_l(t)$ and $\eta^R_l(t)$ and the history dependent dissipation terms given by the integrals. Here $\Sigma^+_L(t) = V^L g^+_L(t) V^{L\dagger}$ and $\Sigma^+_R(t) = V^R g^+_R(t) V^{R\dagger}$ are therefore the self energy corrections to the wire due to the left and the right reservoirs respectively. The properties of the noise and dissipation are easiest to express in Fourier space and are given by:

$$\Sigma^+_L(\omega) = V^L g^+_L(\omega) V^{L\dagger},, \quad \left\langle \tilde{\eta}^{L\dagger}_l(\omega) \tilde{\eta}^L_m(\omega') \right\rangle = [\Gamma_L(\omega)]_{ml} f_L(\omega) \delta(\omega - \omega'), \tag{6}$$

with $\Gamma_L = \frac{1}{2\pi i}(\Sigma^-_L(\omega) - \Sigma^+_L(\omega))$ and $f_L(\omega) = f(\omega, \mu_L, T_L) = [e^{(\omega-\mu_L)/T_L} + 1]^{-1}$ is the usual Fermi-Dirac distribution. The right reservoir will have similar properties.

Results

- **Steady State Solution**

The exact steady state solution of the wire operators in terms of two Green's functions, $G^+_1(\omega)$ and $G^+_2(\omega)$ as,

$$\tilde{c}_m(\omega) = [G^+_1(\omega)]_{ml} \left[\tilde{\eta}^L_l(\omega) + \tilde{\eta}^R_l(\omega) \right] + [G^+_2(\omega)]_{ml} \left[\tilde{\eta}^{L\dagger}_l(-\omega) + \tilde{\eta}^{R\dagger}_l(-\omega) \right],$$

The Green's functions are given by,

$$G^+_1(\omega) = \frac{1}{\Pi(\omega) + K[\Pi^*(-\omega)]^{-1} K^\dagger}, \quad G^+_2(\omega) = G^+_1(\omega) K [\Pi^*(-\omega)]^{-1}. \tag{7}$$

. where,

$$\Pi(\omega) = \omega - H^W - \Sigma^+_L(\omega) - \Sigma^+_R(\omega), \quad \text{and} \quad K = \Delta - \Delta^T \tag{8}$$

$$\tag{9}$$

- **Particle Current and Conductance**

$$J_L = \int_{-\infty}^{\infty} d\omega \Big(T_1(\omega)(f^e_L(\omega) - f^e_R(\omega)) + T_2(\omega)(f^e_L(\omega) - f^h_R(\omega)) + T_3(\omega)(f^e_L(\omega) - f^h_L(\omega)) \Big),$$
$$G_L = T_1(\mu_L) + T_2(\mu_L) + T_3(\mu_L) + T_3(-\mu_L). \tag{10}$$

where,

$$T_1(\omega) = 4\pi^2 \operatorname{Tr}\left[G^+_1(\omega) \Gamma_R(\omega) G^-_1(\omega) \Gamma_L(\omega) \right], \quad T_2(\omega) = 4\pi^2 \operatorname{Tr}\left[G^+_2(\omega) \Gamma^T_R(-\omega) G^-_2(\omega) \Gamma_L(\omega) \right] \text{ and} \tag{11}$$

$$T_3(\omega) = 4\pi^2 \operatorname{Tr}\left[G^+_2(\omega) \Gamma^T_L(-\omega) G^-_2(\omega) \Gamma_L(\omega) \right]. \tag{12}$$

$f^e_L(\omega)$ and $f^h_L(\omega)$ are the electron and hole occupation numbers respectively. On comparison of the expression for particle current with standard Landauer's expressions we see that,

- $T_1(\omega)$ corresponds to normal electrons being transmitted from the left to the right bath (normal transmission)
- $T_2(\omega)$ corresponds to the process of an electron from the left bath being scattered as a hole into the right bath (Andreev transmission)
- $T_3(\omega)$ corresponds to the electron from the left bath scattered back as a hole into the left bath again (Andreev reflection)

- **Energy current and Conductance**

$$J^H_L = \int_{-\infty}^{\infty} d\omega\, \omega \left[T_1(\omega) + T_2(\omega) \right] (f^e_L(\omega) - f^e_R(\omega)). \tag{13}$$

$$G^H_L = \frac{dJ^H_L}{dT_L} = \frac{k_B^2 \pi^2 T_L}{6} G_T(\mu_L), \quad G_T(\mu_L) = 2(T_1(\mu_L) + T_2(\mu_L)) \tag{14}$$

Application to 1-D wires

These results when applied to 1-D models show zero bias peaks whenever the system posses the well known Majorana bound state.

Nearest neighbor chain

$$\mathcal{H}_W = \sum_{j=1}^{N-1} \left[-\mu_w a^\dagger_j a_j + \left(-\eta_w a^\dagger_j a_{j+1} + \Delta a_j a_{j+1} + \text{c.c.} \right) \right]$$

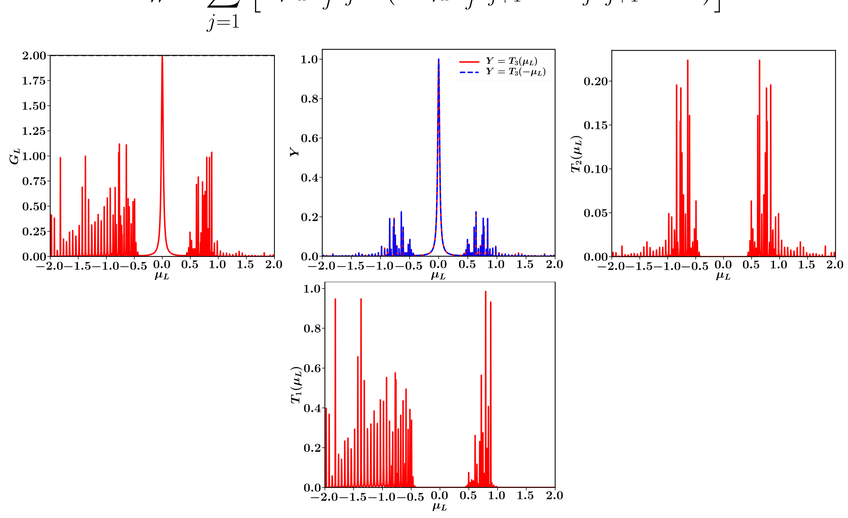

Variation of zero temperature conductance and the terms contributing with, μ_L. Parameter values– $N = 100$, $V_L = V_R = 0.2$, $\eta_w = \mu_w = 1$, $\eta_b = 1$ and $\Delta = 0.25$.

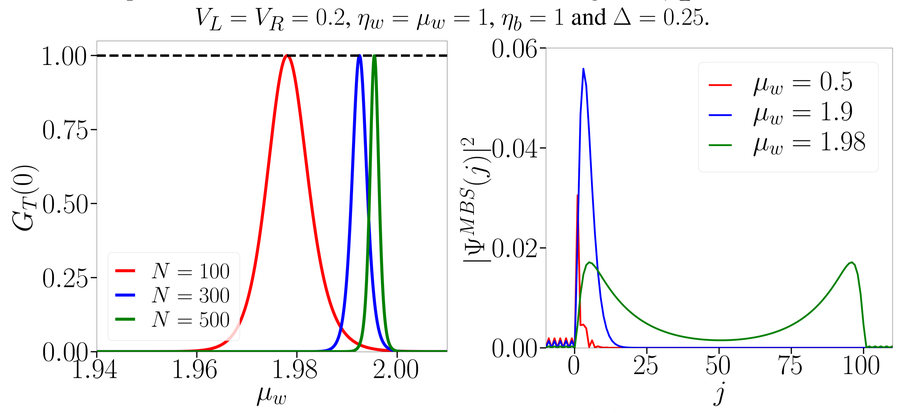

(Left panel) Variation of thermal conductance at $\mu_L = 0$ in units of $\pi^2 k_B^2 T_L/6$ with the chemical potential, μ_w, on the wire for different wire sizes. (Right panel) shows the wave function of the Majorana zero mode for $N = 100$. Parameter values– $V_L = V_R = 0.25$, $\eta_w = \eta_b = 1$ and $\Delta = 0.3$.

Next to nearest neighbor Chain

$$\mathcal{H}^W = \sum_{j=1}^{N} \left[-\mu_w a^\dagger_j a_j - \eta_1 \left(a^\dagger_j a_{j+1} + a_j a_{j+1} + \text{c.c.} \right) - \eta_2 \left(a^\dagger_j a_{j+2} + e^{i\theta} a_j a_{j+2} + \text{c.c.} \right) \right].$$

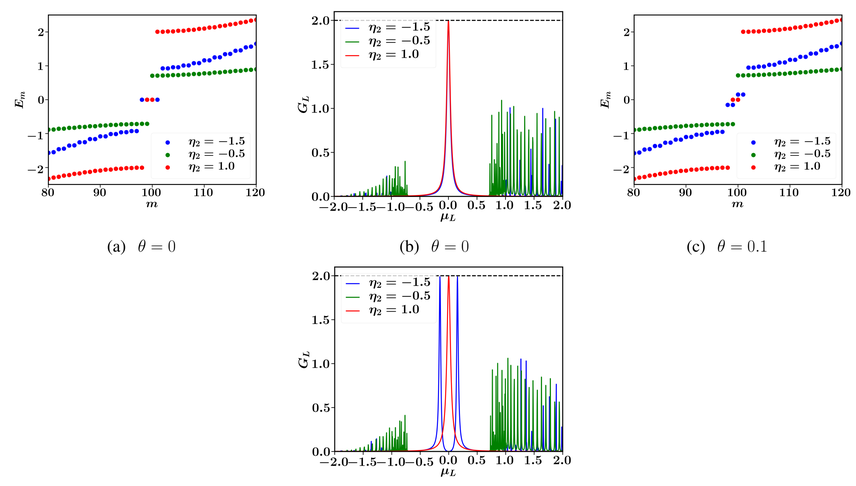

(a) $\theta = 0$ (b) $\theta = 0$ (c) $\theta = 0.1$ (d) $\theta = 0.1$

Figure 1: Conductance and Spectrum plots of a next to nearest neighbor chain. Parameter values $\eta_1 = 1$, $\mu_w = -2$, $N = 100$, $V_L = V_R = 0.3$ and $\eta_b = 1.5$.

Conclusions

- Exact results for Energy current, particle current and corresponding conductance were obtained for a general model of superconducting wire. The expressions of these quantities involve multiple NEGF Transmission coefficients.
- These NEGF Transmission coefficients can also be physically interpreted in terms of scattering processes as normal transmission, Andreev transmission and Andreev reflection.
- The results when applied to 1-D models show zero bias peaks whenever the system is in the topologically non-trivial regime.

References

[1] A. Y. Kitaev, "Unpaired majorana fermions in quantum wires," *Physics-Uspekhi*, vol. 44, no. 10S, p. 131, 2001.

[2] L. Fu and C. L. Kane, "Superconducting proximity effect and majorana fermions at the surface of a topological insulator," *Physical review letters*, vol. 100, no. 9, p. 096407, 2008.

[3] V. Mourik, K. Zuo, S. M. Frolov, and S. Plissard, "Ep a. m. bakkers, and lp kouwenhoven," *Science*, vol. 336, p. 1003, 2012.

[4] A. Das, Y. Ronen, Y. Most, Y. Oreg, M. Heiblum, and H. Shtrikman, "Zero-bias peaks and splitting in an al–inas nanowire topological superconductor as a signature of majorana fermions," *Nature Physics*, vol. 8, no. 12, pp. 887–895, 2012.

[5] Y. Niu, S. B. Chung, C.-H. Hsu, I. Mandal, S. Raghu, and S. Chakravarty, "Majorana zero modes in a quantum ising chain with longer-ranged interactions," *Physical Review B*, vol. 85, no. 3, p. 035110, 2012.

[6] M. Thakurathi, O. Deb, and D. Sen, "Majorana modes and transport across junctions of superconductors and normal metals," *Journal of Physics: Condensed Matter*, vol. 27, no. 27, p. 275702, 2015.

A Theory of Resistivity in Kondo Lattice Materials: Memory Function Approach

Komal Kumari [1], Raman Sharma[2],Navinder Singh[3]

[12]*Department of Physics, Himachal Pradesh University Shimla HP-India*

[3]*Physical Research Laboratory, Ahmedbad-Gujart India*

Email:[1]komalphy.hpu@gmail.com, [2] raman.sharma@hpuniv.ac.in, [3]navinder@prl.res.in

Abstract

We have theoretically analysed D.C. resistivity (ρ) in the Kondo-lattice materials using the powerful memory function formalism. The complete temperature evolution of ρ is investigated using the Wölfle-Götze expansion of the memory function. The resistivity in this model originates from spin-flip magnetic scattering of conduction s-electron off the quasi-localized d or f electron spins. We find the famous resistivity upturn in lower temperature regime ($k_BT << \mu_d$), where μ_d is the effective chemical potential of d-electrons. In the high temperature regime ($\mu_d << k_BT$) we discover that resistivity scales as cube root of T ($\rho \propto T^{\frac{3}{2}}$).

Introduction

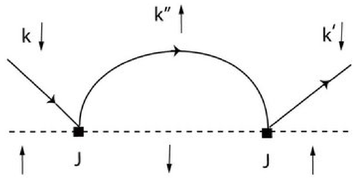

Figure 1 Represents scattering mechanism of conduction and localized electrons spin. http://www.scholarpedia.org/article/Kondo effect.

Mathematical Formulation

$$H_{sd} = \frac{J}{N}\sum_{k'k}\Big\{a^\dagger_{k'\uparrow}a_{k\downarrow}S^-(k'-k) + a^\dagger_{k'\downarrow}a_{k\uparrow}S^+(k'-k) + (a^\dagger_{k'\uparrow}a_{k\uparrow} - a^\dagger_{k'\downarrow}a_{k\downarrow})S^z(k'-k)\Big\} \quad (1)$$

In Kubo's linear response theory, the dynamical conductivity is given by

$$\sigma_{\mu\nu}(\omega) = V\int_0^\infty dt e^{i\omega t}\int_0^\beta d\lambda\langle J_\mu(-i\hbar\lambda)J_\nu(t)\rangle. \quad (2)$$

Mori-Zwanzig projection operator technique rewrites the Kubo formula as

$$\sigma_{\mu\nu}(z) = i\frac{\omega_p^2}{4\pi}\frac{1}{z + M_{\mu\nu}(z)}. \quad (3)$$

Within the Götze-Wölfle approach the memory function is computed using the equation of motion method and a perturbative expansion of the memory function[1], [2].

$$M(z) \simeq \frac{1}{z}(\frac{ne^2}{m})[\langle\langle \dot{J}_1;\dot{J}_1\rangle\rangle_z - \langle\langle \dot{J}_1;\dot{J}_1\rangle\rangle_0], \qquad \dot{J}_1 = -\frac{i}{\hbar}[J_1, H] \quad (4)$$

$$H = H_0 + H_{sd} \qquad J_1 = \frac{1}{V}\sum_{k\sigma} ev_k a^\dagger_{k\sigma}a_{k\sigma}, \quad \phi(z) = \langle\langle \dot{J}_1;\dot{J}_1\rangle\rangle \quad (5)$$

$$\phi(z) = \frac{-e^2J^2}{N^2\hbar^2V^2}\sum_{k'k}\sum_{pp'}\Big(v_1(k') - v_1(k)\Big)\Big(v_1(p) - v_1(p')\Big)\langle\langle a^\dagger_{k'\uparrow}a_{k\downarrow}S^-(k'-k) + a^\dagger_{k'\downarrow}a_{k\uparrow}S^+(k'-k)\ ;\ a^\dagger_{p'\uparrow}a_{p'\downarrow}S^-(p-p') + a^\dagger_{p\downarrow}a_{p'\uparrow}S^+(p-p')\rangle\rangle. \quad (6)$$

Correlator can be computed

$$\phi(z) = \langle\langle \dot{J}_1;\dot{J}_1\rangle\rangle = i\frac{V}{\hbar}\int_0^\infty e^{izt}\langle\ [\dot{J}_1(t);\dot{J}_1(0)]\ \rangle dt. \quad (7)$$

The time dependence of operators explicitly as $a^\dagger_{k'\uparrow}(t) = e^{\frac{i\epsilon_{k'}t}{\hbar}}a^\dagger_{k'\uparrow}(0)$ for s-band mobile electrons. For d-band density operators we write $S^-(k'-k,t) = e^{-i\omega_{k'-k}t}S^-(k'-k,0)$ and dispersion of the magnetic excitation is taken in the form of $\hbar\omega_q \propto q^2$.

$$M(z) = -\frac{J^2m}{N^2\hbar^3nV\omega}\sum_{k'k}(v_1(k') - v_1(k))^2\Big\{f^s_{k'}(1-f^s_k)\sum_{k_d,k'_d}(f^d_{k_d} - f^d_{k'_d}) - (f^s_k - f^s_{k'})\sum_{k_d,k'_d}f^d_{k_d}(1-f^d_{k'_d})\Big\}\Big[\frac{1}{\frac{\epsilon_{k'}}{\hbar} - \frac{\epsilon_k}{\hbar} - \omega_{k'-k} + z} + \frac{1}{\frac{\epsilon_{k'}}{\hbar} - \frac{\epsilon_k}{\hbar} - \omega_{k'-k} - z} - \frac{1}{\frac{\epsilon_{k'}}{\hbar} - \frac{\epsilon_k}{\hbar} - \omega_{k'-k}} - \frac{1}{\frac{\epsilon_{k'}}{\hbar} - \frac{\epsilon_k}{\hbar} - \omega_{k'-k}}\Big] \quad (8)$$

Identity $\lim_{\eta\to 0}\frac{1}{a\mp i\eta} = \mathfrak{P}(\frac{1}{a}) \pm i\pi\delta(a)$ transforms the expression to

$$M''(\omega) = \frac{J^2\pi V}{3N^2mn}\int_0^\infty\frac{dq}{\omega}\,q^2\int_0^\infty\frac{d^3k}{(2\pi)^3}\int_0^\infty\frac{d^3k'}{(2\pi)^3}\delta(\vec{q} - |\vec{k'} - \vec{k}|) F(f^s_k, f^s_{k'}, f^d_{k_d}, f^d_{k'_d})[\delta(\epsilon_{k+q} - \epsilon_k - \hbar\omega_q + \hbar\omega) - \delta(\epsilon_{k+q} - \epsilon_k - \hbar\omega_q - \hbar\omega)]. \quad (9)$$

$$M''(\omega) = \frac{1}{4\pi^3}\frac{J^2Vm^2}{3N^2\hbar^8n}\int_0^{q_D}\frac{dqq^2q}{k_s^2\omega}\int_0^\infty\sqrt{\epsilon}d\epsilon\int_0^\infty d\epsilon'\sqrt{\epsilon'}\{f^s_{k+q}(1-f^s_k) \sum_{k_d}(f^d_{k_d} - f^d_{k_d+q}) - (f^s_k - f^s_{k+q})\sum_{k_d}f^d_{k_d}(1-f^d_{k_d+q})\} [\delta(\epsilon_{k+q} - \epsilon_k - \hbar\omega_q + \hbar\omega) - \delta(\epsilon_{k+q} - \epsilon_k - \hbar\omega_q - \hbar\omega)]. \quad (10)$$

In DC limit under assumptions $k_BT \ll \mu_s$ and $\hbar\omega_q \ll \mu_s$,

$$M''(T) = \frac{1}{12\pi^3}\frac{J^2V^2m^2}{N^2\hbar^7n}\mu_s\Big\{\frac{1}{8\pi^2}(\frac{q_D}{q_s})^6q_s^5\frac{\sqrt{\lambda}}{\sqrt{\beta\mu_s}}\Big(\int_{-\beta\mu_d}^\infty dx\sqrt{x+\beta\mu_d}\frac{e^x}{(e^x+1)^2} + \frac{2}{3}\int_{-\beta\mu_d}^\infty dx(x+\beta\mu_d)^{\frac{3}{2}}\frac{e^x}{(e^x+1)^2} - \frac{4}{3}\int_{-\beta\mu_d}^\infty dx(x+\beta\mu_d)^{\frac{3}{2}}\times \frac{e^{2x}}{(e^x+1)^3}\Big) + \frac{1}{8\pi^2}(\frac{q_D}{q_s})^6q_s^5(\frac{\lambda}{\beta\mu_s})^{\frac{3}{2}}\int_{-\beta\mu_d}^\infty dx\sqrt{x+\beta\mu_d}\frac{e^x}{(e^x+1)^2}\Big\}. \quad (11)$$

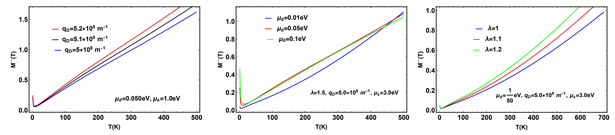

Figure 2. $M''(T)$ for various values of q_D taking $\lambda = 1.5$. second presents $M''(T)$ for various values of μ_d at $\lambda = 1.5$. Notice the upturn in the low temperature limit. The curve for $\mu_d = 0.05eV$ and $\mu_d = 0.1eV$. The reason is that $\mu_d = 0.01eV$ corresponds to the temperature $T = \frac{\mu_d}{k_B} \simeq 120K$, thus the high temperature $T^{\frac{3}{2}}$ scaling shows its effect on the scale shown in the figure. Right shows high temperature behaviour of $M''(T)$ for three different values of $\lambda = 1.0$ $\lambda = 1.1$ *and* $\lambda = 1.2$.

Results

Case 1: Low temperature limit ($k_BT \ll \mu_d$)

$$M''(T) \simeq \frac{1}{12\pi^3}\frac{J^2V^2m^2}{N^2\hbar^7n}\mu_s\Big[\frac{1}{8\pi^2}(\frac{q_D}{q_s})^6q_s^5\sqrt{\lambda}\Big(\sqrt{\frac{\mu_d}{\mu_s}}\int_{-\beta\mu_d}^\infty dx\frac{e^x}{(e^x+1)^2} + \frac{2}{3}\frac{\mu_d^{\frac{3}{2}}}{\sqrt{\mu_s}}\frac{1}{k_BT}\int_{-\beta\mu_d}^\infty dx\Big\{\frac{e^x}{(e^x+1)^2} - 2\frac{e^{2x}}{(e^x+1)^3}\Big\}\Big) + \frac{1}{8\pi^2}(\frac{q_D}{q_s})^4q_s^5(\frac{\lambda}{\mu_s})^{\frac{3}{2}}k_BT\sqrt{\mu_d}\int_{-\beta\mu_d}^\infty dx\frac{e^x}{(e^x+1)^2}\Big]. \quad (12)$$

$$M''(T\to 0) \sim \frac{1}{T}f_s(T), \quad f_s(T) = \int_{-\beta\mu_d}^\infty dx\Big\{\frac{e^x}{(e^x+1)^2} - 2\frac{e^{2x}}{(e^x+1)^3}\Big\}, \quad (13)$$

Case 2: High temperature limit ($k_BT \gg \mu_d$)

$$M''(k_BT \gg \mu_d) \sim \mathbb{C}\ T^{\frac{3}{2}}\int_0^\infty dx\sqrt{x}\frac{e^x}{(e^x+1)^2} \sim 0.536\ \mathbb{C}\ T^{\frac{3}{2}}$$
$$M''(k_BT \gg \mu_d) \sim T^{\frac{3}{2}}. \quad (14)$$

Comparison with experimental data

Resistivity formula $\rho(T) = \frac{m}{ne^2}\frac{1}{\tau(T)} = \frac{m}{ne^2}M''(T)$

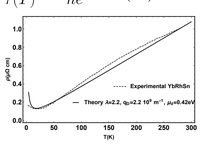

figure 3 represents theory comparison with resistivity of compound $YbRhSn$ [3], [4]. We observe best fit for $\lambda = 2.2, q_D = 2.2\times10^9m^{-1}$ and $\mu_d = 0.42eV$. Lattice constanta $= 6.925\AA, c = 3.984\AA$, $\mu_s = 7.7eV$, $q_s = 1.43\times10^9m^{-1}$ and number density $n = 9.961\times10^{28}m^{-3}$.

References

[1] W. Götze and P. Wölfle, "Homogeneous dynamical conductivity of simple metals," *Phys. Rev. B*, vol. 6, pp. 1226–1238, 4 Aug. 1972. DOI: 10.1103/PhysRevB.6.1226. [Online]. Available: https://link.aps.org/doi/10.1103/PhysRevB.6.1226.

[2] N. Singh, *Electronic transport theories: From weakly to strongly correlated materials*. CRC Press, 2017.

[3] D. Kaczorowski, A. Leithe-Jasper, P. Rogl, H. Flandorfer, T. Cichorek, R. Pietri, and B. Andraka, "Magnetic, thermodynamic, and electrical transport properties of ternary equiatomic ytterbium compounds YbTM (T=transition metal, M=Sn and Bi)," *PRB*, vol. 60, no. 1, pp. 422–433, Jul. 1999. DOI: 10.1103/PhysRevB.60.422.

[4] T. Jeong, "Electronic structure and magnetism of *YbRhSn*," *The European Physical Journal B-Condensed Matter and Complex Systems*, vol. 53, no. 2, pp. 213–217, 2006.

Structural and Magnetization Studies of Cu, Mn co-doped Franklinite

Suchit Kumar Jena[1], A. K. Hota[1], S. Ghosh[1], M. Roy Chowdhury[1], Maruthi R.[1], and S. Thota[1*]
Department of Physics, Indian Institute of Technology Guwahati, Guwahati-781039, Assam, India

Introduction

- Ferrimagnetic Spinel $Cu_{0.2}Zn_{0.8}Fe_{2-x}Mn_xO_4$ has a general formula: $(A_xB_{1-x})_A[A_{1-x}B_{1+x}]_BO_4$;$(0 \leq x \leq 1)$
- Its unit cell is made up of 32-Oxygen atoms, 8-A atoms, and 16-B atoms.

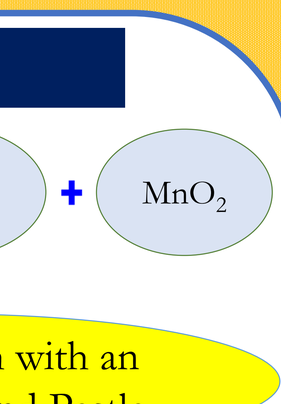

Applications

(i) Magnetic storage media
(ii) Catalyst production
(iii) Gas-sensors
(iv) Super-capacitors
(v) Li-ion batteries

I-V measurement

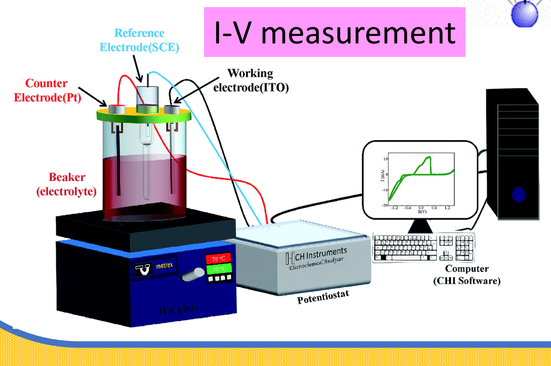

Magnetic storage media

Methodology

CuO + ZnO + Fe_2O_3 + MnO_2

Synthesis

Grinded for 5h with an Agate mortar and Pestle

Solid State Method

Pressed into 13 mm dia pellets

Sintered at 1200°C

Regrinded and resintered

$Cu_{0.2}Zn_{0.8}Fe_{2-x}Mn_xO_4$ -Bulk

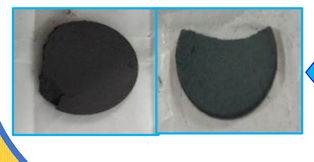

Advantages of Solid State Reaction

- Homogeneous dispersion of dopants
- Controls the composition accurately
- Yields in a stable product
- No toxic waste is produced

Theory

- Néel's expression for ferrimagnets:
  $(1/\chi) = (T/C) + (1/\chi_0) - [\sigma_0 / (T- \Theta)]$
- Fisher's relation: $C_M \sim d(\chi T)/dT$
- Curie-law:
  $(\mu_{eff} / \mu_B)^2 = 3k_B\chi T / N_A\mu_B^2$

References

[1] *J. Electron. Mater.* **47**, 3608 (2018).
[2] *J. Appl. Phys.* **128**, 073908 (2020).
[3] *J. Appl. Phys.* **113**, 203905 (2013).
[4] *Phys. Rev. B* **99**, 134422 (2019).

Acknowledgement

S. K. Jena acknowledges the FIST programme of the Department of Science and Technology, India, for partial support of this work (Ref. No. SR/FST/PSII-020/2009).

Results and Discussion

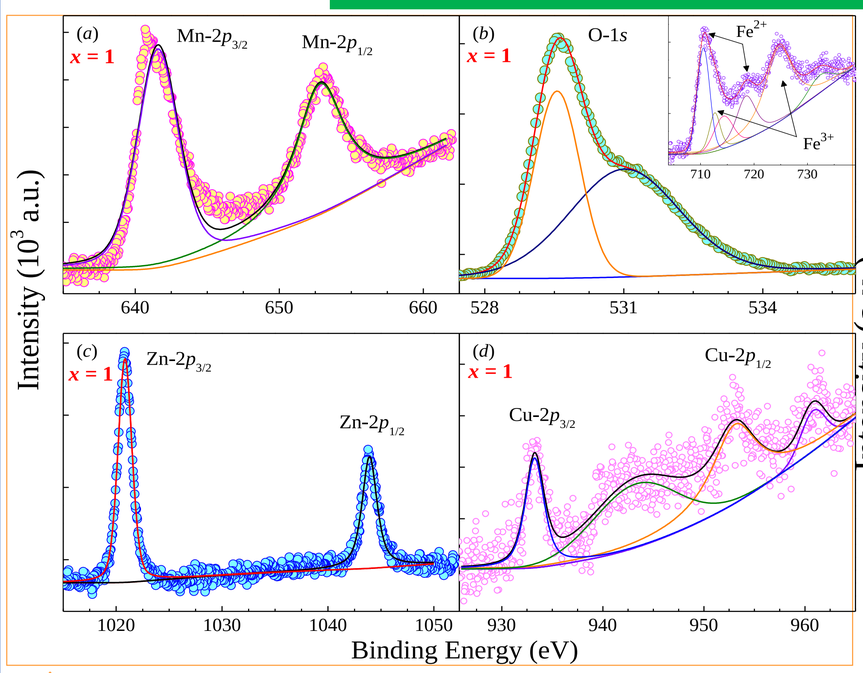

XPS spectra

M vs T

XRD pattern

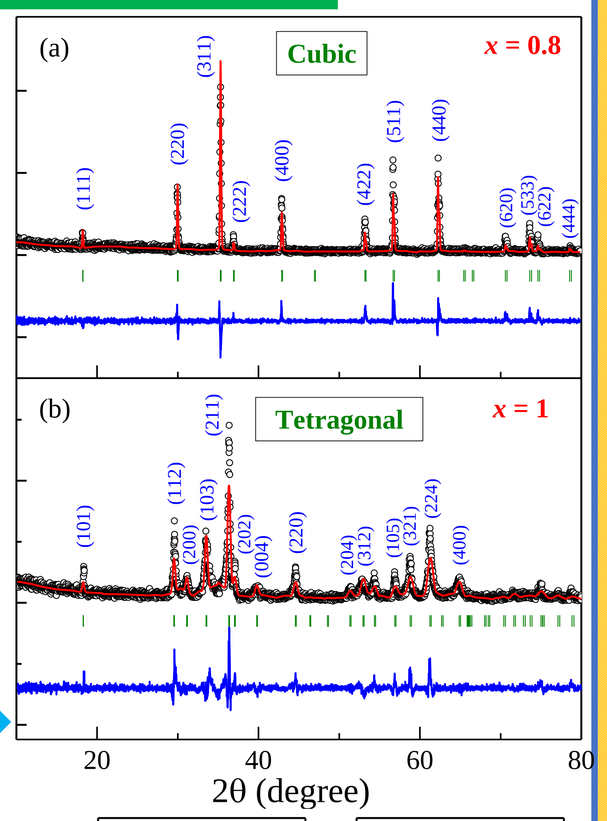

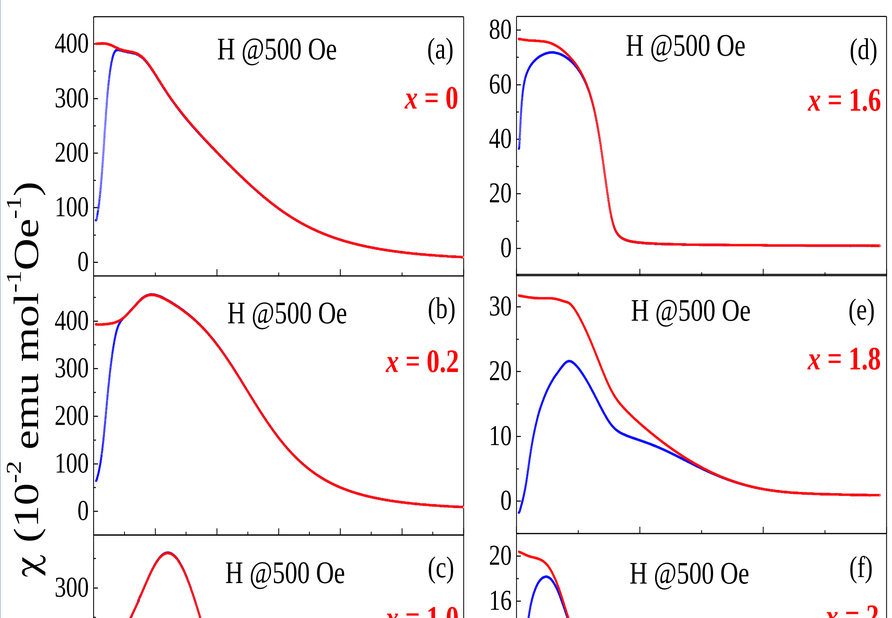

Néel Fit

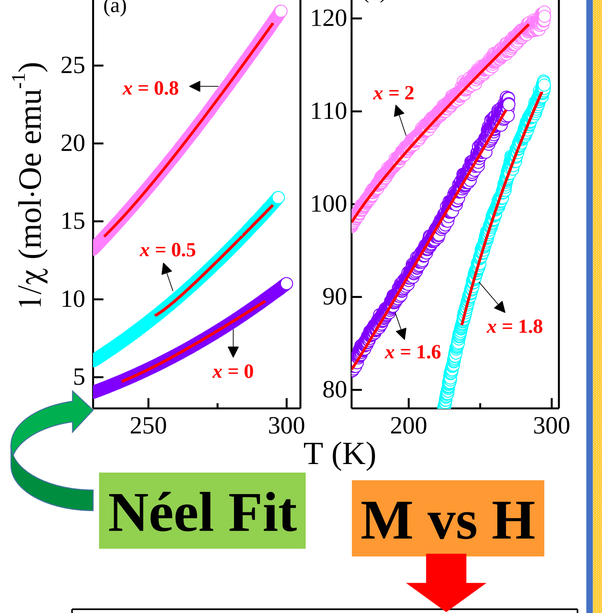

M vs H

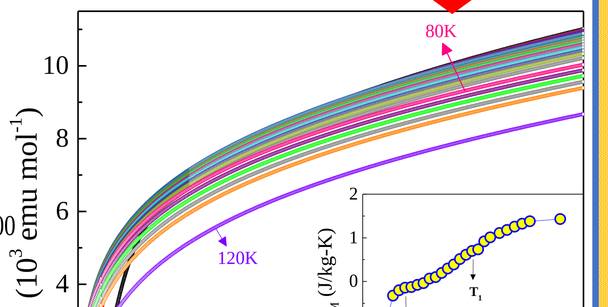

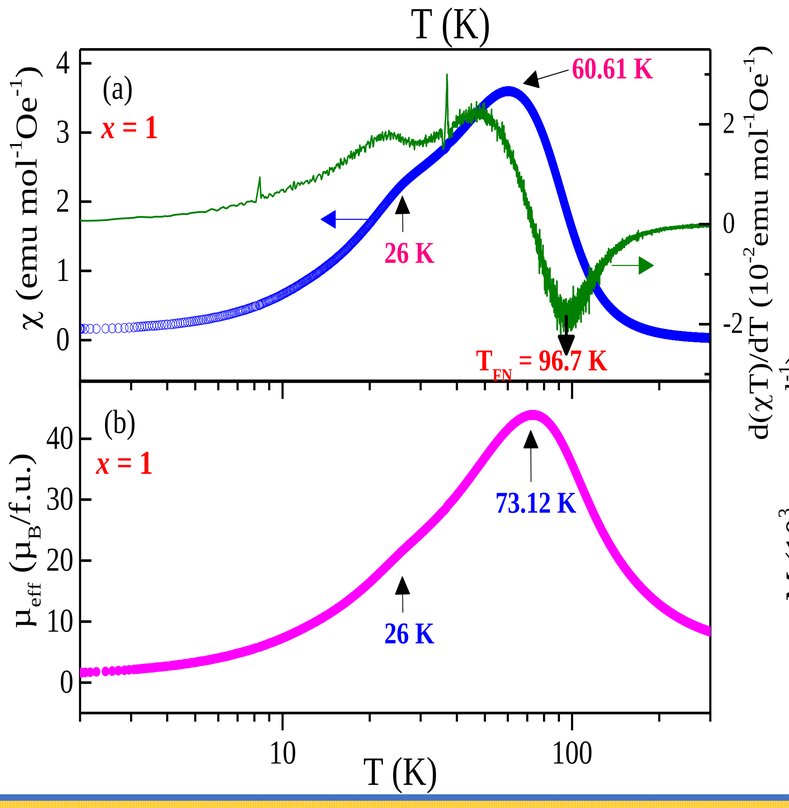

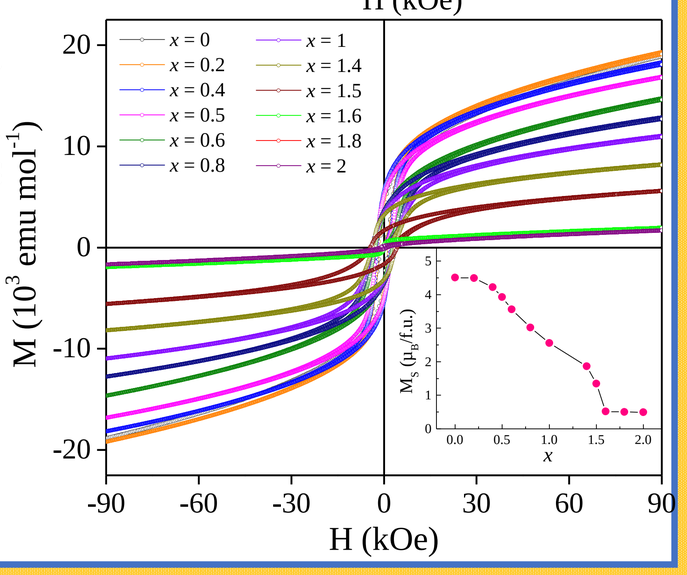

Conclusions

- Cations present in the system: Cu^{2+}, Zn^{2+}, Fe^{2+}, Fe^{3+}, Mn^{3+}, O^{2-}.
- The system exhibits mixed spinel Cubic phase (Fd–$3m$) for $0 \leq x \leq 0.8$ and Tetragonal phase ($I4_1/amd$) for $1 \leq x \leq 2$.
- Néel fits confirms ferrimagnetic ordering (T_{FN}) in all x.
- Three GT (Gabay and Toulouse) transitions are observed in all the compounds owing to the geometrical frustration arising due to competing exchange interaction between Mn and Fe cations.

Plasmon-Phonon Coupled Modes in Quantum Wire System

Devi Puttar[1,*], Vishal Verma[1], Akariti Sharma[2] and Vinayak Garg[1]

[1]*Department of Physics, Punjabi University, Patiala-147 002, India*

[2]*Physical Research Laboratory, Ahmedabad-380 009, India*

[*]Email: bhattdev2112@gmail.com

INTRODUCTION

- Due to the advancement in nanotechnology, it has now become possible to fabricate ultra-narrow and clean semiconductor-based electron quantum wire structures, and to perform a great number of experimental and theoretical studies to explore their electronic properties.
- In these quantum wires, the motion of electrons is free only in one spatial direction and confined in the two transverse directions quantum mechanically.
- There are many interesting quantum effects observed in these systems [1-2] primarily due to the strong electron-electron (*e-e*) correlation effects. Besides, the interaction of electrons to the underlying lattice in terms of phonons is also important as it contributes in addition to usual *e-e* interactions.
- Therefore, to better understand and compare the theoretical results with the experimental/simulation findings, the electron-phonon (*e-ph*) interactions should also be included in addition to *e-e* correlations.
- In a doped polar semiconductor wherein most of the quantum wire structures are fabricated, coupling of free electrons takes place with the longitudinal-optical (LO) phonons of the underlying lattice *via* the Fröhlich interaction potential, resulting in a quasiparticle called a polaron.
- The *e-ph* interactions (polaronic effects) in quasi-one-dimensional electron gas (Q1DEG) as realized in quantum wires have been theoretically studied over the years by several authors [3-7].
- In this work, we study the effect of *e-ph* interactions along with the usual *e-e* interactions on the collective excitation energy *i.e.* plasmons of an electron quantum wire at absolute zero. The *e-e* interactions (exchange-correlations) will be dealt using the STLS theory, while the electron LO-phonon interactions *via* the Fröhlich coupling.

THEORETICAL FORMALISM

- In this work, we consider an electron quantum wire at absolute zero in which the electrons are coupled to longitudinal optical (LO) phonons.
- Electrons in the wire interact among themselves through the Coulomb potential and through virtual LO-phonon exchange *via* the Fröhlich interaction. The Fourier transform of bare Coulomb interaction potential for the harmonic confinement of electrons in the (cylindrical) quantum wire is expressed as

$$V_{e-e}(q) = \frac{e^2}{2\varepsilon_\infty} f(qb); \tag{1}$$

- The LO-phonon-mediated electron-electron (*e-e*) interactions are both wave vector and frequency dependent, described by the Fröhlich interaction potential as [4]

$$V_{e-ph}(q,\omega) = M_q^2 D_0(\omega). \tag{2}$$

- In Eq. (2), M_q is the effective one-dimensional (1D) Fröhlich interaction matrix element given by

$$M_q^2 = V_{e-e}(q)\frac{\omega_{LO}}{2}\left[1-\frac{\varepsilon_\infty}{\varepsilon_0}\right], \tag{3}$$

and $D_0(\omega)$ is the unperturbed retarded bare LO-phonon propagator given as

$$D_0(\omega) = \frac{2\omega_{LO}}{\omega^2-\omega_{LO}^2}. \tag{4}$$

ω_{LO} is the LO-phonon frequency and $\varepsilon_0(\varepsilon_\infty)$ is the static (high frequency) background lattice dielectric constant.

- To study the collective excitation energy *i.e.* plasmon-phonon coupled modes of an electron-phonon (*e-ph)* coupled quantum wire system, we use the dielectric formulation within the linear response theory.
- Here, the dynamic density response function $\chi(q,\omega)$ is the quantity of central importance as the plasmon energy of the quantum wire can easily be obtained from it**.** In the Singwi, Tosi, Land and Sjölander (STLS) theory [8], the density response function is given as

$$\chi(q,\omega) = \frac{\chi_0(q,\omega)}{1-V_T(q,\omega)[1-G(q)]\chi_0(q,\omega)}, \tag{5}$$

where $V_T(q,\omega)$ is the total (bare) interaction potential describing the *e-e* and *e-ph* interactions as

$$V_T(q,\omega) = V_{e-e}(q) + V_{e-ph}(q,\omega), \tag{6}$$

- $\chi_0(q,\omega)$ in Eq. (5) is the non-interacting density response function of 1D electrons at absolute zero given by [2]

$$\chi_0(q,\omega) = -\frac{2}{\hbar}\int_{-\infty}^{+\infty}\frac{dp}{h}\frac{f^0\left(p+\frac{\hbar q}{2}\right)-f^0\left(p-\frac{\hbar q}{2}\right)}{\omega-\frac{pq}{m^*}+i\eta}. \tag{7}$$

- In Eq. (5), $G(q)$ is the local-field correction (LFC) factor which gives correction to the total bare interaction potential $V_T(q,\omega)$ due to exchange-correlations among the 1D electrons and is obtained as

$$G(q) = -\frac{1}{n}\int_{-\infty}^{\infty}\frac{dq'}{2\pi}\frac{q'}{q}\frac{V(q')}{V(q)}[S(q-q')-1], \tag{8}$$

- *S*(*q*) is the static structure factor of the electron quantum wire which is related to the imaginary part of $\chi(q,\omega)$ through the fluctuation-dissipation theorem as

$$S(q) = -\frac{\hbar}{\pi n}\int_0^\infty d\omega\, \chi(q,i\omega). \tag{9}$$

Here, we transform the ω-integration to the imaginary ω-axis *i.e.* $\omega \to i\omega$ in $\chi(q,\omega)$ through Wick's rotation.

- The collective excitation energies (plasmon-phonon coupled modes) can be calculated from the poles of $\chi(q,\omega)$ *i.e.* by setting denominator of $\chi(q,\omega)$ equal to zero in Eq. (5) as

$$1 - V_T(q,\omega)[1-G(q)]\chi_0(q,\omega) = 0. \tag{10}$$

DIMENSIONLESS SYSTEM OF UNITS

- For numerical calculations, it is convenient to work in a dimensionless system of units.
- q is taken in the units of Fermi wave vector k_F, ω, ω_{LO} and ω_{TO} are expressed in the units of Fermi energy E_F.
- The transverse wire width b in the effective Bohr atomic radius $a_0^*[= \varepsilon_\infty\hbar^2/(m^*e^2)]$.
- The linear electron number density *n* is described by a dimensionless parameter $r_s = 1/(2na_0^*)$; $n = N/L$ (Total no. of electrons per unit length). Throughout our calculations, we take $\hbar$ equal to unity.
- We use the physical parameters corresponding to a *GaAs* based electron quantum wire system *i.e.* $\omega_{LO} = 36.8\ meV$, $\omega_{TO} = 33.8\ meV$ $1\ Ryd^* = 7.67 meV$, $m^* = 0.067 m_e$ and $\varepsilon_0(\varepsilon_\infty) = 12.9\ (10.9)$.

RESULTS AND DISCUSSION

- In this Section, we report our numerical results for the plasmon-phonon (*pl-ph*) coupled modes of an electron quantum wire system at absolute zero, fixed wire width *b* and different electron number density parameter r_s.
- To calculate the *pl-ph* coupled modes along with the exchange correlations of an electron quantum wire, the set of Eqs. (5), (8) and (9) is solved numerically in a self-consistent manner within a predefined tolerance of 10^{-7} at the chosen *q*-points.

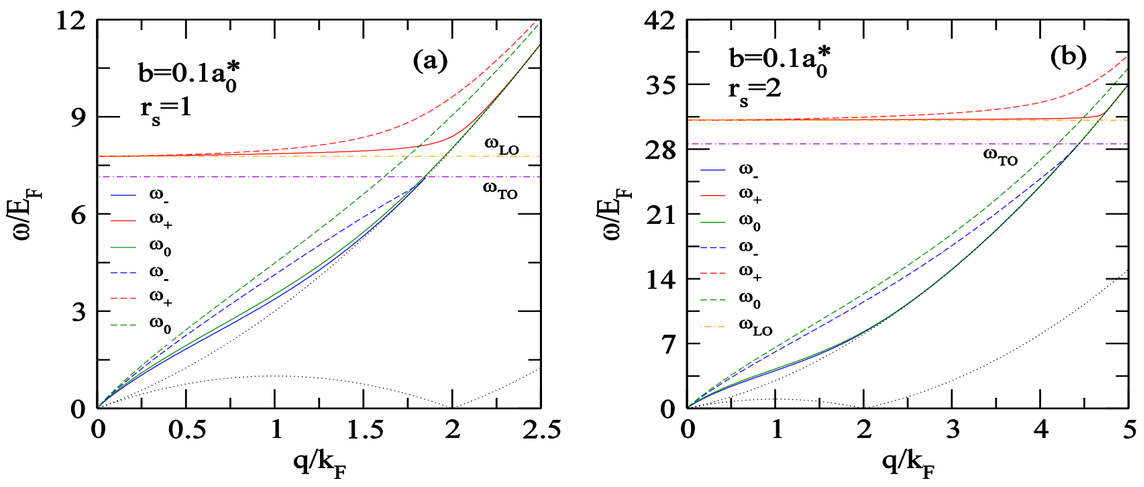

FIG.1: Collective excitation energy $\omega(q)/E_F$ as a function of q/k_F for $r_s = 1$ [in panel (a)] and $r_s = 2$ [in panel (b)], at wire width $b = 0.1a_0^*$ in STLS (solid lines) and RPA (dashed lines). ω_+ and ω_- represent the upper and lower branches of the plasmon-phonon excitation energy. ω_0 is the plasmon dispersion without the *e-ph* interactions. The dotted lines are the boundaries of *e-h* pair continuum and dash-dotted lines represent the ω_{LO} and ω_{TO} energy.

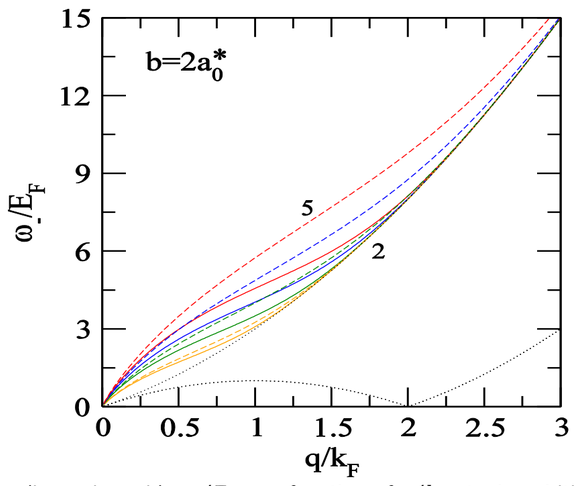

FIG. 2: Collective excitation energy (lower branch) ω_-/E_F as a function of q/k_F at wire width $b = 2a_0^*$ in STLS (solid lines) and RPA (dashed lines) for $r_s = 2$, 3, 4 and 5 with the consideration of *e-ph* interactions. Dotted lines present the boundary of *e-h* pair continuum.

- The numerical results for plasmon-phonon (*pl-ph)* coupled modes ($\omega(q)$) in quantum wire system are reported for $r_s = 1$ in Fig. 1(a) and $r_s = 2$ in Fig. 1(b), at $b = 0.1a_0^*$.
- We observe that the inclusion of *e-ph* interactions causes the plasmon-*LO*-phonon collective excitation energy spectrum to split into two branches, one with energy lower and other with energy higher than the *LO* phonon energy.
- The lower branch of energy ω_- starts from the origin at smaller value of q, goes to ω_{TO} and upper branch ω_+ starts from ω_{LO} and meets with the electron-hole (*e-h*) pair continuum for sufficiently large value of q.
- This branching in the plasmon energy is observe only when we deal with the combine effect of both *e-ph* as well as *e-e* interactions.
- For comparison, we also show the RPA results for the *pl-ph* coupled modes in quantum-wire system.
- We also depict the results for the true plasmon modes *i.e.* plasmon energy ω_0 due to the only *e-e* interaction effects which has usually a single branch.
- In order to highlight the effect of exchange correlations along with the *e-ph* interactions, in Fig. 2 the numerical results are depicted for collective excitation energy *i.e.* lower branch of *pl-ph* coupled modes ω_- in STLS and RPA schemes at $b = 2a_0^*$ for $r_s = 2, 3, 4$ and 5.
- It is clearly seen that RPA overestimate the energy modes ω_- and also, the inclusion of *e-ph* coupling significantly affects the short-range correlations in the electron quantum wire system.

CONCLUSIONS

- We have theoretically investigated the role of *e-ph* coupling along with the usual *e-e* interactions on the collective excitation energy of an electron quantum wire at absolute zero using the STLS theory.
- The *e-ph* interactions affect the collective excitation energy to such an extent that their inclusion slightly splits the plasmon-*LO*-phonon energy spectrum into two branches, with one branch having energy lower and other have higher energy than the *LO* phonon energy.
- Interestingly, we observe that the lower branch of energy *i.e.* ω_- get soften as comparison to the true plasmon energy *i.e.* ω_0 and at large value of q, ω_0 meets with the ω_+ modes.
- This demonstrates the importance of inclusion of *e-ph* coupling in addition to the usual *e-e* interactions.

REFERENCES

1. O. M. Auslaender, H. Steinberg, A. Yacoby, Y. Tserkovnyak, B. I. Halperin, K. W. Baldwin, L. N. Pfeiffer and K. W. West, Science 308, 88 (2005); V. V. Deshpande and M. Bockrath, Nat. Phys. 4, 314 (2008).
2. V. Garg, R. K. Moudgil, K. Kumar and P. K. Ahluwalia, Phys. Rev. B 78, 045406 (2008); K. Kaur, A. Sharma, V. Garg and R. K. Moudgil, J. Phys.: Condens. Matter 32, 335403 (2020); Vinayak Garg and R. K. Moudgil, Physica E 47, 217 (2013).
3. L. Wendler, R. Haupt and R. Pechstedt, Phys. Rev. B 43, 14669 (1991).
4. E. H. Hwang and S. Das Sarma, Phys. Rev. B 52, R8668 (1995); E. H. Hwang, Ben Yu-Kuang Hu and S. Das Sarma, Phys. Rev. B 54, 4996 (1996).
5. B. Tanatar, J. Phys.: Condens. Matter 5, 2203 (1993); N. Mutluay and B. Tanatar, J. Appl. Phys. 80, 4484 (1996); C. R. Bennett and B. Tanatar, Phys. Rev. B 55, 7165 (1997).
6. A. N. Borges, F. A. P. Osório, P. C. M. Machado and O. Hipólito, Mod. Phys. Lett. B 13, 819 (1999).
7. P. C. M. Machado, F. A. P. Osório and A. N. Borges, Microelectronics Journal 34, 529 (2003); *ibid.* Braz. J. Phys. 36, 391 (2006); *ibid.* Physica Status Solidi B 248, 931 (2011); *ibid.* Int. J. of Mod. Phys. B 30, 1650218 (2016).
8. K. S. Singwi, M. P. Tosi, R. H. Land and A. Sjölander, Phys. Rev. 176, 589 (1968).

Self Consistent Renormalization (SCR) Theory of Itinerant Magnetism

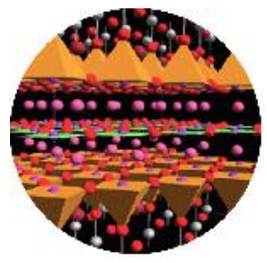

Akariti Sharma*,1, Bharathiganesh* and Navinder Singh*

**Physical Research Laboratory Ahmedabad-380009,Gujarat,India*

[1]*akaritisharma@gmail.com*

Introduction

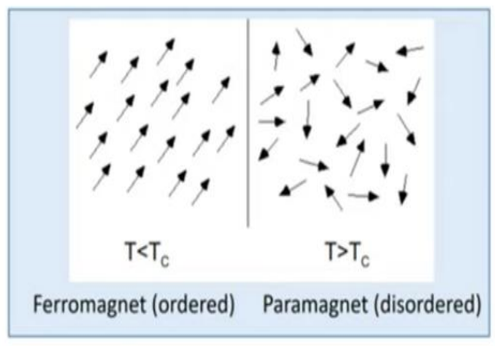

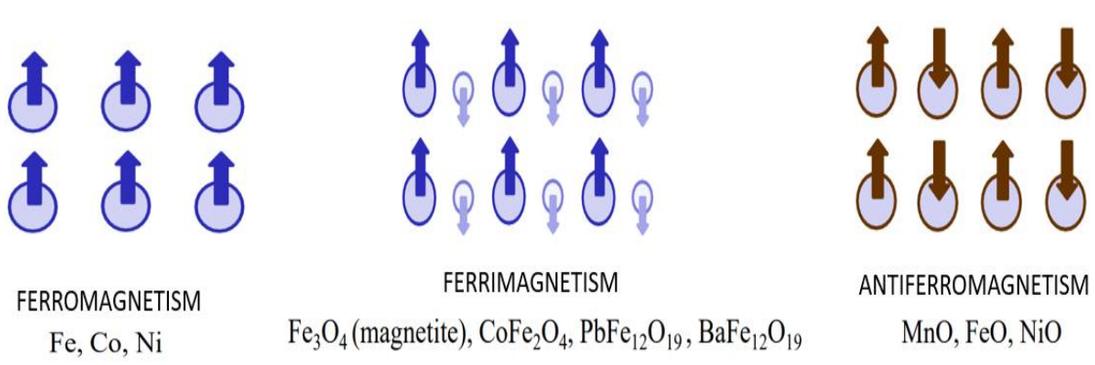

Theoretical Formalism for Magnetic Susceptibility

The magnetic susceptibility is given by:

$$\chi = \left[\left(\frac{\delta^2 F(M)}{\delta M^2}\right)^{-1}\right]_{M=M^*} \quad (1)$$

With *M* is magnetization and *N* is the total number of electrons.

$$M = N_\downarrow - N_\uparrow \; ; \; N = N_\downarrow + N_\uparrow$$

F(M) is the total free energy and is a function of M.

The partition function of the system in the presence of magnetic field is given by

$$Z(H) = Tr\left[e^{\frac{-[\mathcal{H}+HM_z]}{K_B T}}\right] \quad (2)$$

here *H* is the magnetic field aligned along the z-axis, *H* is the Hamiltonian of the system and *Mz* is the component of magnetization along *H*. Therefore, the free energy of the system is given as

$$F(H) = -TlnZ(H) \quad (3)$$

further, the free energy can be expressed in terms of *M* by using the Legendre transformation in the following way

$$Z(M) = \frac{1}{2\pi i}\int_{-i\infty-\epsilon}^{i\infty+\epsilon} d\left(\frac{H}{T}\right) e^{\left(-\frac{H}{T}\right)M} Z(H) \quad (4)$$

Therefore *F(M)* is the free energy for a given value of M and is obtained as

$$F(M) = -TlnZ(M) \quad (5)$$

Self-Consistent Scheme

$$\delta = \chi_0/\alpha\chi = 2/I\chi = (1-\alpha+\lambda)/\alpha.$$

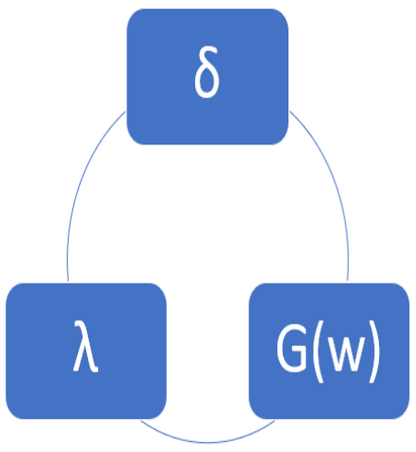

$$\lambda(T) = \frac{1}{2\pi}\int_{-\infty}^{+\infty} d\omega coth\left(\frac{1}{2}\beta\omega\right) G(\omega)$$

$$G(\omega) = -\xi(4\pi)^{-1} Im \int dq \left\{\alpha f_0 \left(\partial^2 f_0/\partial B^2\right)(\delta + 1 - f_0)^{-1} + (\partial f_0/\partial B)^2 (\delta + 1 - f_0)^{-2}\right\}$$

Results

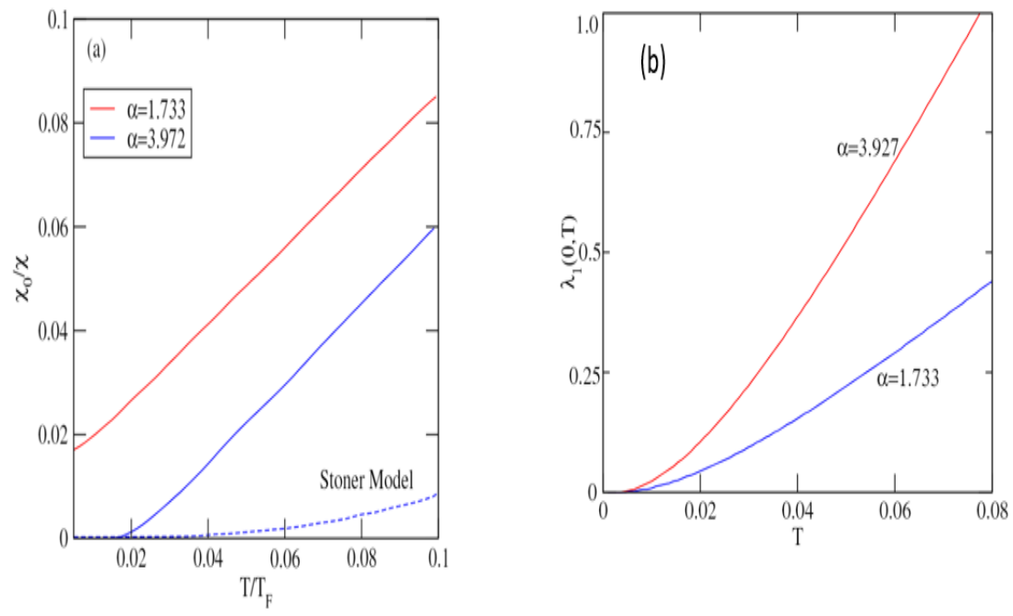

Key Points:

- χ_0/χ (renormalized Susceptibility) vs. T plots are found to be linear in T-linear and follow Curie-Weiss Law above Tc.
- Correlation effects and spin fluctuations are found to be increased with increase in α and so as Tc.
- It seen that Stoner Model underestimate the value of renormalized susceptibility due to the over estimation of spin fluctuations at particular value of α so as Tc.
- $\lambda_1(0,T)$ is strongly T-dependent part of the correction factor, and found to increases with increase in temperature.
- Increase in $\lambda_1(0,T)$ with T indicating the reduction in effective spin fluctuations . The study of T-dependence of $\lambda_1(0,T)$ is most important in SCR theory as it overcome the Stoner contribution and χ_0/χ is much closer to Curie-Weiss susceptibility at α=1.733.
- Greater will be the interactions in the system greater will be the amplitude of these spin fluctuations in the system.

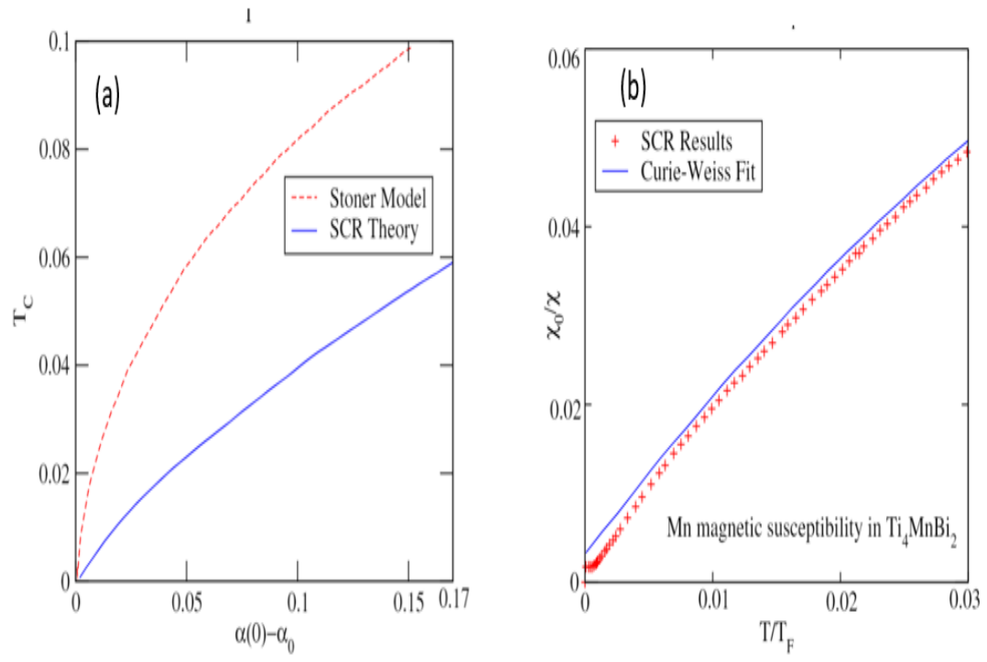

Key Points:

- T_C vs. $\alpha(0)-\alpha_0$ curves shows that the calculated T_C values based on the SCR theory are small, while overestimated values are obtained by the Stoner model.
- It is seen that the this lowering in T_C is due to the inclusion of spin-fluctuations by adding the correction factor.
- In order to check the validly of our calculations, we planed to apply SCR theory for realistic systems. So far, we opt Ti_4MnBi_2 compound and calculate the renormalized susceptibility for Mn in this system and also compared it with Curie-Weiss Fit.
- It is observed that our calculated results are in qualitative agreement with the recent published data. (https://doi.org/10.1103/PhysRevB.102.014406).

Conclusions

- Stoner Theory is based on the Hartree-Fock" Mean Field" approximation (Only the exchange term is taken into account and the Correlation terms are neglected).
- Random Phase Approximation (RPA) goes ahead of the Stoner Theory by including the correlation effects. It gives an aid to study the dynamical effects like stoner-excitation, spin-wave etc. using the dynamical Magnetic Susceptibility χ(q,ω).
- There is an additional free energy due to the correlation effects which is not taken into account in the RPA theory. This extra free energy will be expressed in terms of the transverse dynamical susceptibility using the fluctuation dissipation theorem.
- Self Consistent Renormalization (SCR) theory takes into account this neglected free energy and in doing so it goes beyond the RPA Theory.
- Thus the SCR theory leads to a serious modification of the results obtained through RPA theory.
- The calculated value of Tc (using SCR Theory) agrees well with the experiments for weakly ferro-magnetic and anti-ferromagnetic systems.
- It reproduces the Curie-Weiss law well.

Coulomb Drag in Coupled Electron-Electron Quantum Wire System at Finite-Temperature in the RPA

Vishal Verma[1, *], Devi Puttar[1], Akariti Sharma[2], Vinayak Garg[1, #]
[1]Department of Physics, Punjabi University, Patiala-147 002, India
[2]Physical Research Laboratory Ahmedabad, India
[#]Email: vinayak2000@gmail.com

INTRODUCTION

- Recent developments in the semiconductor growth technology and the modern fabrication techniques have led to the fabrication of very high-quality one-dimensional (1D) quantum structures to explore the various aspects of particle interactions in these systems [1-2].
- In 1D systems, the confinement of motion of the quantum particles (electrons or holes) is done in such a way that they can move only in one spatial direction.
- In addition to isolated (single) 1D electron systems, presently, there is a great deal of theoretical and experimental interest to explore the coupled 1D electron systems separated by a distance of few nanometers. These systems are popularly known as coupled quantum wire systems and here the charge carriers may be electrons or holes.
- In coupled quantum wire systems, the two wires are placed at a sufficiently small inter-wire distance of the order of few nanometers. Here, the energy and momentum transfer across the wires (without the actual contact) is known to influence the transport properties of the individual quantum wire.
- There are many new and interesting physical phenomena observed in coupled quantum wire systems such as Wigner crystallization, Coulomb drag [3-9] and charge-density-wave (CDW) instability etc.
- Coulomb drag is such a theoretically predicted [3-5] and an experimentally observed [6-9] phenomenon in coupled quantum wire systems wherein, current in one wire drives the same in the other. The Coulomb drag effect may also be used as a probe to investigate the localization properties of coupled quantum systems.
- In this work, we calculate the Coulomb drag rate between the electrons in coupled electron-electron quantum wire system as a function of temperature and particle number density by applying the random-phase approximation (RPA).

COUPLED ELECTRON-ELECTRON QAUNTUM WIRE MODEL

- In this work, we consider a coupled electron-electron quantum wire system with each wire having width b and inter-wire spacing $d(>b)$, the Fourier transform of interaction potential $V_{ll'}(q)$ among electrons is given as

$$V_{ll'}(q) = \frac{2e^2}{\varepsilon_0} K_0\left(q\sqrt{b^2 + (1-\delta_{ll'})d^2}\right), \quad (1)$$

with l and l' as the wire indices *(l = 1, 2)*. ε_0 is the dielectric constant of the background wire material (same for both the wires). $K_0(x)$ is the zeroth-order modified Bessel's function of the first kind.

- We employ the dielectric formulation within the framework of linear response theory wherein the coupled electron-electron system is perturbed by weak space-time dependent external electric potential and the density response function is calculated.

THEORETICAL FORMALISM

- To study the Coulomb drag effect in coupled electron-electron quantum wire system, we will use the expression for the drag rate derived through the Boltzmann equation [3-5].
- The **Coulomb drag rate τ_D^{-1}** for two parallel quantum wires is given by

$$\tau_D^{-1} = \frac{1}{4\pi m^* n T} \int_0^\infty q^2 dq \times \int_0^\infty |W_{12}(q,\omega:\mu,T)|^2 \times \frac{Im\chi_1^0(q,\omega;\mu,T) Im\chi_2^0(q,\omega;\mu,T)}{sinh^2\left(\frac{\omega}{2T}\right)} d\omega. \quad (2)$$

Where m^* is the electron effective mass and n is the linear electron number density. '1' and '2' are the wire indices. $Im\chi_l^0(q,\omega;\mu,T)$ is the imaginary part of the 1D temperature dependent density response function of *'l'* wire.

- Here $W_{12}(q,\omega;\mu,T)$ *is* the dynamically screened inter-wire interaction potential which is given as

$$W_{12}(q,\omega;\mu,T) = \frac{V_{12}(q)}{\epsilon(q,\omega;\mu,T)} \quad (3)$$

- In Eq. (3), the dielectric function $\epsilon(q,\omega;\mu,T)$ for coupled quantum wire system is expressed as

$$\epsilon(q,\omega;\mu,T) = [1 - V_{11}(q)\chi_1^0(q,\omega;\mu,T)][1 - V_{22}(q)\chi_2^0(q,\omega;\mu,T)] - [V_{12}(q)]^2\chi_1^0(q,\omega;\mu,T)\chi_2^0(q,\omega;\mu,T) \quad (4)$$

- The density response function $\chi_l^0(q,\omega;\mu,T)$ of 1D non-interacting electrons in 'l' wire at finite-temperature and is related to $\chi_l^0(q,\omega;\mu,T=0)$ by Maldague's method [10] and can be written as

$$\chi_l^0(q,\omega;\mu,T) = \begin{cases} \int_{e^{(-\mu/k_BT)}}^1 \chi_l^0(q,\omega;\mu + k_BT\, ln|x|, T=0)\frac{dx}{(1+x)^2} + \\ \int_0^1 \chi_l^0(q,\omega;\mu - k_BT\, ln|x|, T=0)\frac{dx}{(1+x)^2};\ \mu > 0 \\ \int_0^{e^{(\mu/k_BT)}} \chi_l^0(q,\omega;\mu - k_BT\, ln|x|, T=0)\frac{dx}{(1+x)^2};\ \mu < 0 \end{cases} \quad (5)$$

Where μ is the chemical potential and k_B is Boltzmann constant.

DIMENSIONLESS SYSTEM OF UNITS

- We work in dimensionless system of units in which q is taken in the units of the Fermi wave vector k_F.
- Chemical potential μ and ω in Fermi energy E_F , Temperature T in Fermi temperature *($\tau = T/T_F$)*.
- Wire width b and inter-wire spacing d in the effective Bohr atomic radius a_{0e}^* *[$=\varepsilon_0 \hbar^2/(m_e^* e^2)$]*.
- The linear electron number density n is described by a dimensionless parameter $r_s = 1/(2na_{0e}^*)$ and $n = N/L$ (Total no. of electrons per unit length of the wire).
- Throughout our calculations we take ε_0, k_B, $\hbar$ equal to unity.

RESULTS AND DISCUSSION

- In this section, we report our results for the Coulomb drag rate as a function of temperature and electron number density for different values of inter-wire separation in the RPA.
- In the calculation of drag rate, the inter-wire interaction potential $W_{12}(q,\omega;\mu,T)$ plays a very crucial role. We assume that the inter-wire interaction potential is statically screened i.e. $W_{12}(q,0;\mu,T) = V_{12}(q) / \varepsilon(q,0;\mu,T)$.
- The calculation of $W_{12}(q,0;\mu,T)$ requires computation of $V_{12}(q)$ and $\varepsilon(q,0;\mu,T)$. In turn, $\varepsilon(q,0;\mu,T)$ can be obtained by setting $\omega = 0$ in Eq. (4).

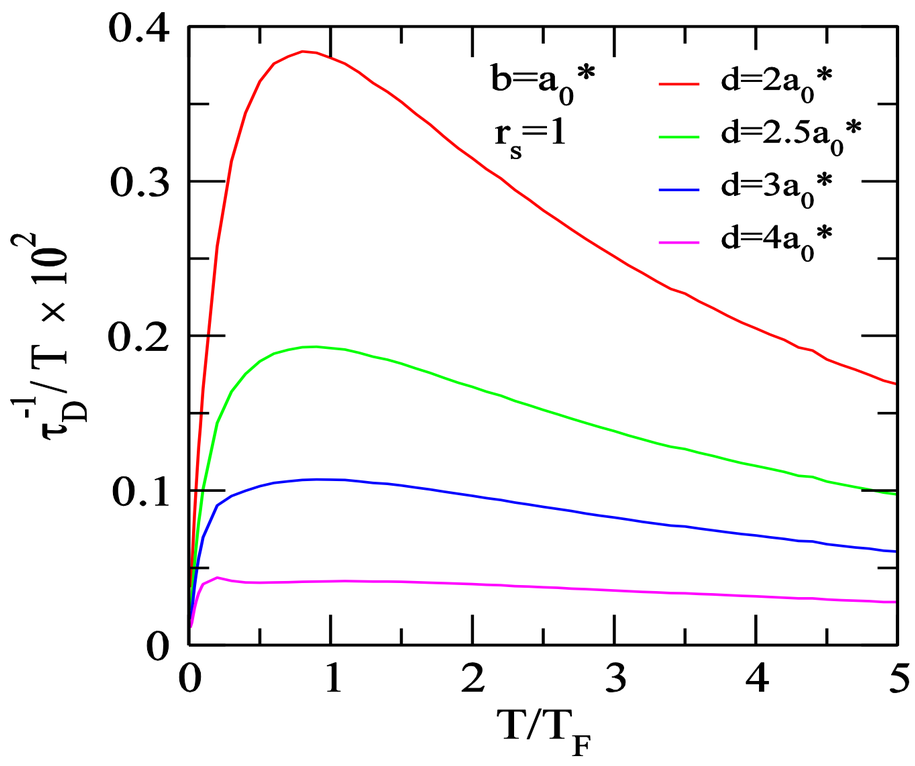

FIG. 1. The scaled drag rate τ_D^{-1}/T plotted as a function of temperature for coupled electron-electron quantum wire system in the random-phase approximation (RPA) at indicated values of inter-wire separation for $b=a_0^*$ and $r_s = 1$.

- Fig. 1. shows the temperature dependence of scaled drag rate τ_D^{-1}/T in the RPA for coupled electron-electron quantum wire system with each wire having width $b=a_0^*$ and $r_s = 1$. We observe that τ_D^{-1}/T has a non-monotonic T-dependence i.e. it first increases and then decreases with rise in T for all separations. The scaled drag rate peaks are observed around $T \sim 0.2 - 0.6\ T_F$ for all separations.
- For sufficiently small d, τ_D^{-1}/T shows a peaked structure at a finite-T which grows stronger and shifts towards higher T with further decrease in d.

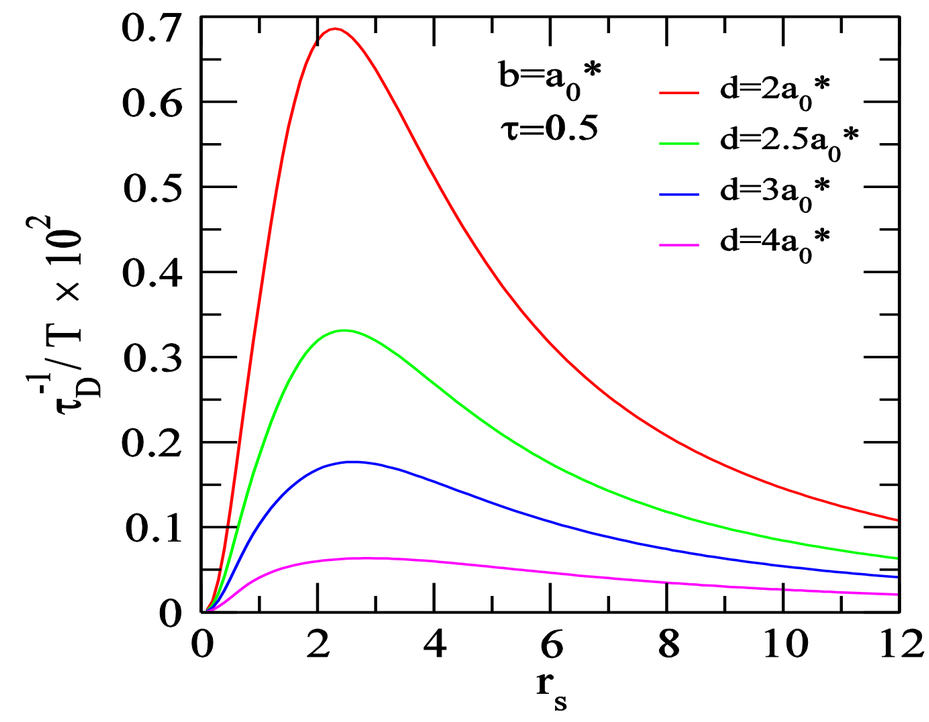

FIG. 2. The scaled drag rate τ_D^{-1}/T plotted as a function of electron number density (r_s) for $b=a_0^*$ and $\tau = 0.5$ at indicated values of inter-wire separation in the RPA.

- In Fig. 2, we show the scaled drag rate τ_D^{-1}/T as a function of r_s at fixed wire width and temperature. It can be clearly seen that with increase in r_s , τ_D^{-1}/T first increases and then decreases and magnitude of τ_D^{-1}/T is maximum for $d=2a_0^*$.
- The increase in τ_D^{-1}/T is due to increases in coupling i.e., r_s among electrons.

CONCLUSIONS

- We have theoretically calculated the temperature and particle number density dependence of scaled drag rate for different values of inter-wire separation in the RPA. It is observe that, with decrease in inter-wire separation the scaled drag rate τ_D^{-1}/T increases.
- It is believed that the RPA becomes less reliable for electron densities $r_s > 1$ (low density). Therefore, it is very important to include the exchange-correlation effects to have a better understanding of Coulomb drag effect in coupled quantum wire systems.

REFERENCES

1. A. Isihara, *Condensed Matter Physics* (Dover Publications, 1991).
2. Paul Harrison, *Quantum Wells, Wires and Dots* (John Wiley and Sons Ltd., 2001).
3. B. Tanatar, Solid State Commun. **99**, 1 (1996).
4. B. Tanatar, J. Appl. Phys. **81**, 6214 (1997).
5. B. Tanatar, Turk. J. Phys. **24**, 143 (2000).
6. P. Debray, P. Vasilopoulos, O. Raichev, R. Perrin, M. Rahman, and W. C. Mitchel, Physica E **6**, 694 (2000).
7. P. Debray, V. Zverev, O. Raichev, R. Klesse, P. Vasilopoulos, and R. S. Newrock, J. Phys.: Condens. Matter **13**, 3389 (2001).
8. P. Debray, V. N. Zverev, V. Gurevich, R. Klesse, and R. S. Newrock, Semicond. Sci. Technol. **17**, R21 (2002).
9. D. Laroche, G. Gervais, M. P. Lilly, and J. L. Reno, *Nature nanotechnology* **6**, 793 (2011).
10. P. F. Maldague, Surf. Sci. **73**, 296 (1978).

Specific heat, EPR and magnetic field dependence of Néel temperature in the manganocolumbite $MnNb_2O_6$

Maruthi R[1], Mohindar S. Seehra[2], Sayandeep Ghosh[1], Rohit Medwal[3] and Subhash Thota[1*]

[1]Department of Physics, Indian Institute of Technology, Guwahati, Assam 781039, India

[2]Department of Physics & Astronomy, West Virginia University, Morgantown, West Virginia 26506, USA

[3]National Institute of Education, Nanyang Technological University Singapore, 637616 Singapore

Introduction

- $MnNb_2O_6$ belongs to the columbites family with **orthorhombic** crystal structure (space group **Pbcn-D^{14}_{2h}**) with 4 molecular formula units per unit cell [1,2,4].
- A Columbite unit cell made up of **24** oxygen atoms, **4-Mn** atoms, and **8-Nb** atoms.
- The **Mn** (divalent) and the **Nb** (pentavalent) ions form separate ***bc***-planes with isosceles triangular arrangement and these ions are stacked as **-Mn-Nb-Nb-Mn-Nb-Nb-Mn-** along the ***a***-axis [4].
- The coordination number is **6** for both Mn^{2+} and Nb^{+5} ions.
- In this structure, staggered zig-zag chains are formed by **MnO_6** and **NbO_6** octahedra along ***c***-axis by sharing their edges.

UNIT CELL:

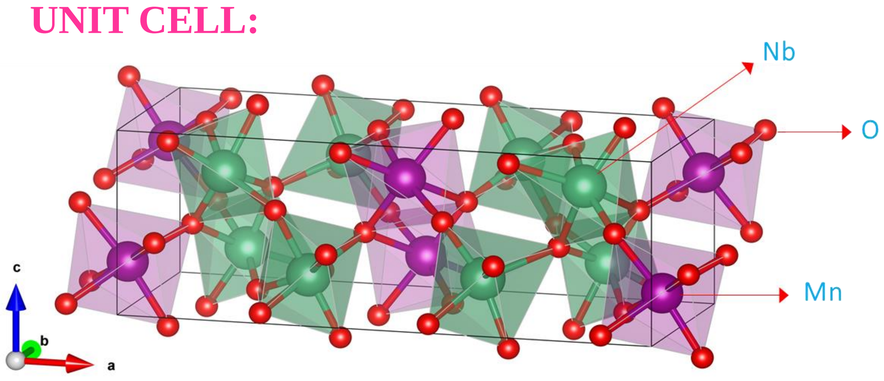

Orthorhombic

$a \neq b \neq c$

$\alpha = \beta = \gamma = 90°$

Octahedral site

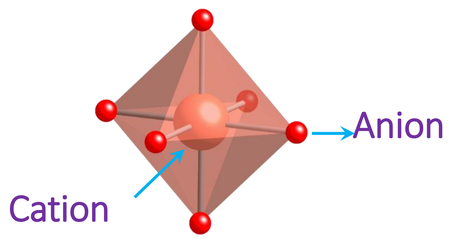

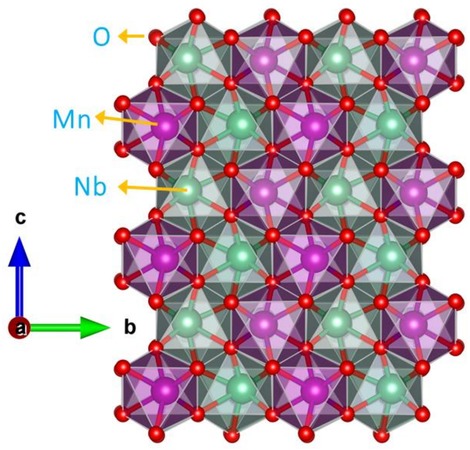

Synthesis of $MnNb_2O_6$

Solid State Reaction

Stoichiometric amounts

MnO_2 + Nb_2O_5

Grinded for 5 hrs

Pressed into pellets

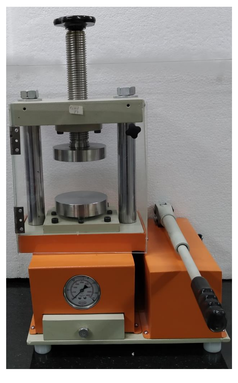

Sintered at 1150°C (12 hrs.) and 1200°C (24 hrs.) in air

$MnNb_2O_6$ synthesized

Result and discussions

XRD pattern

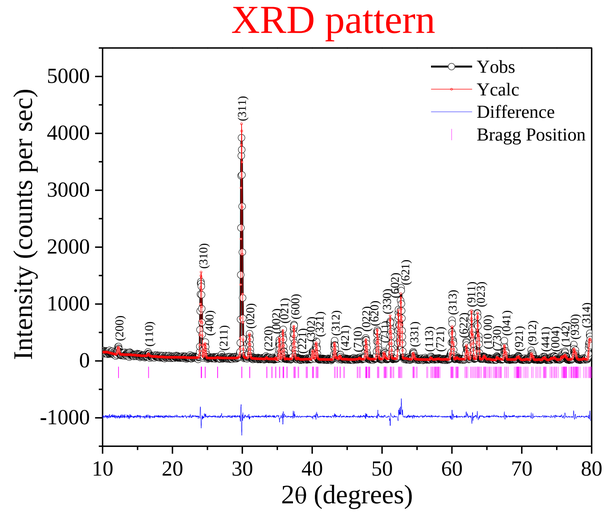

FESEM IMAGE

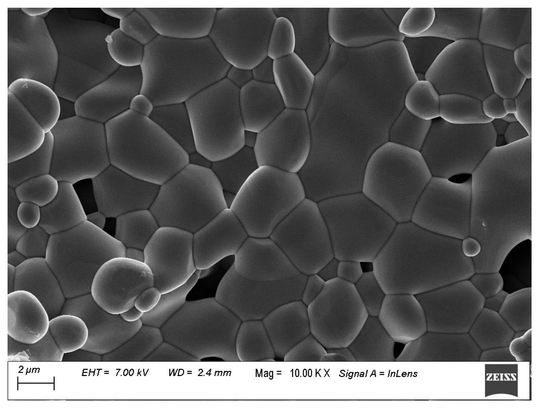

Specific heat & Temperature and field dependence of magnetization:

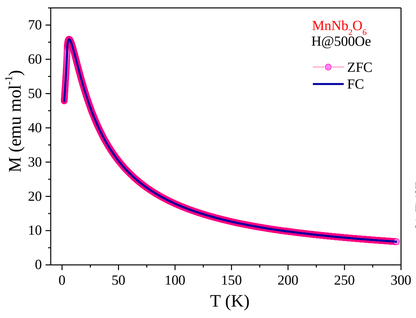

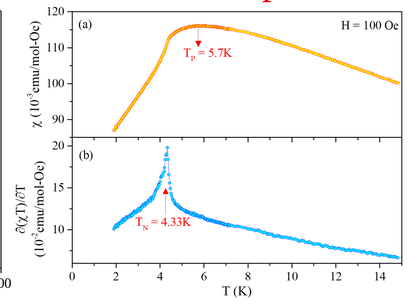

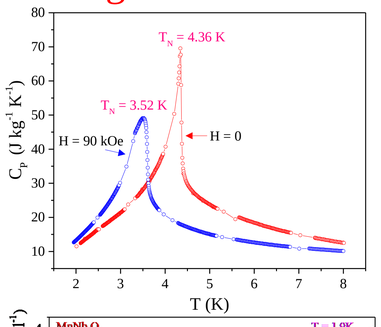

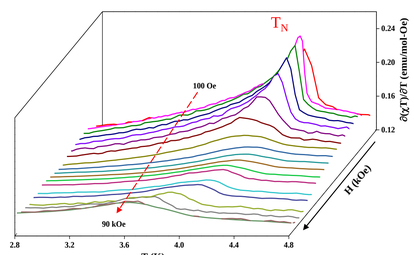

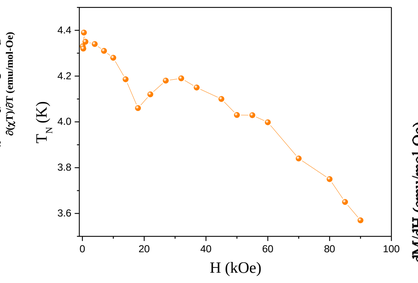

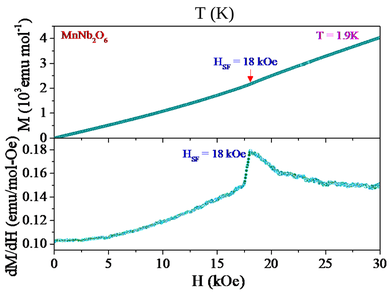

EPR measurements:

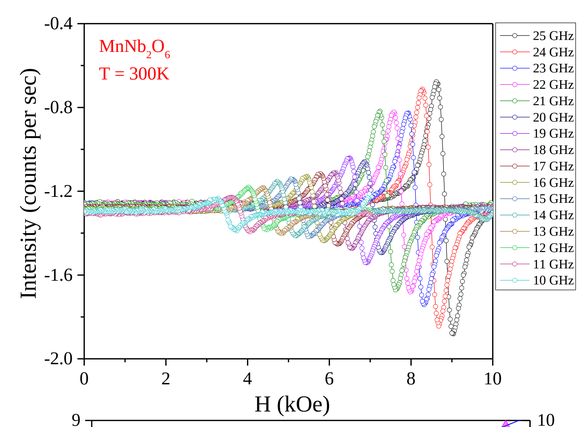

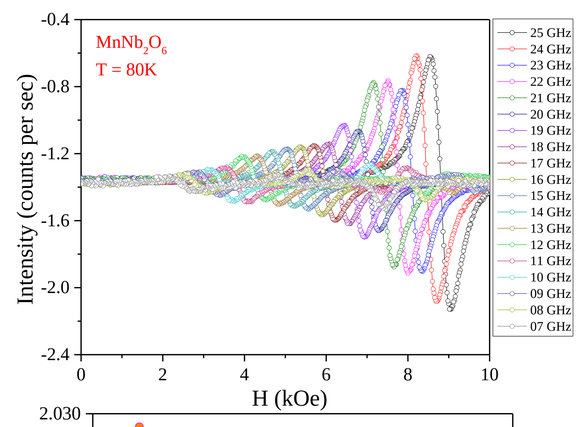

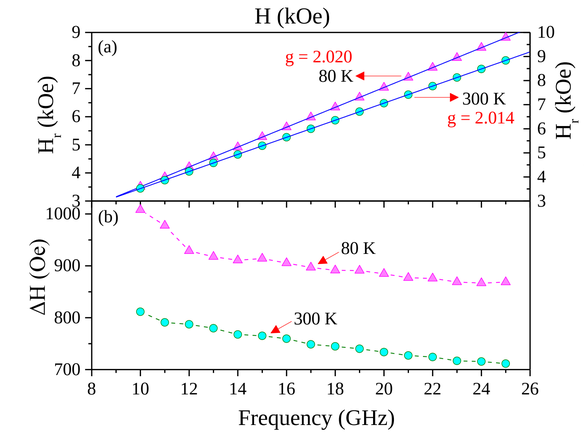

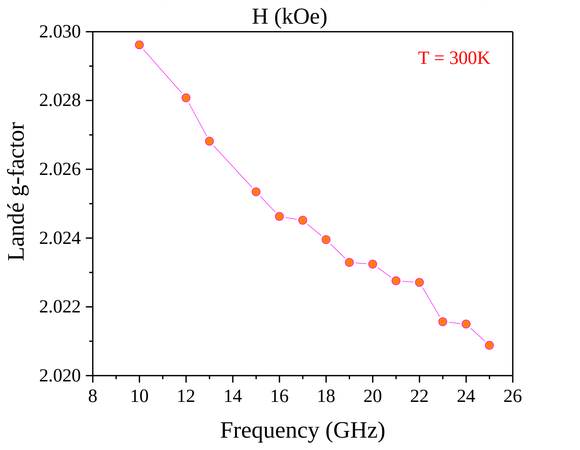

Summary of Results

- The system orders antiferromagnetically below T_N = 4.36 K, in agreement with previous reported T_N = (4.40 ± 0.05) K by Nielson et al [1,2] and Holmes et al [3].
- The specific heat data yields T_N = 4.36 K which is in line with magnetic measurements.
- The Néel temperature T_N shows decrease with magnetic field (H).
- The field dependent magnetization curve at 1.9 K shows a field induced transition nearly H_{SF} = 18kOe
- The obtained average g-values are 2.020 and 2.014 for 80K and 300K respectively from EPR spectrum.
- The g-values at 300 K for Mn^{2+} ion decreases from 2.0296 to 2.0208 as the frequency increases.

References

[1] O. V. Nielsen and A. A. Ballman, J. Magn. Magn. Mater. 1, 320 (1976).
[2] O. V. Nielsen and B. Lebech, J. Phys. C: Solid State Phys. 9, 2401 (1976).
[3] L. M. Holmes and R. R. Hecker, Solid State Commun. 11, 409 (1972).
[4] I. Yaeger and B. M. Wanklyn, Phys. Rev. B 15, 1465 (1977).

PLD grown super-lattices of $[La_{0.7}Sr_{0.3}MnO_3/LaNiO_3]_{10}$ Super-lattices and Characterizations

S. Das[1], R. G. Tanguturi[2], R. K. Dokala[1], S. Ghosh[1], S. Thota [1]

[1] Department of Physics, Indian Institute of Technology Guwahati-781039, Assam, India

[2] School of Materials Science and Engineering, Hubei University, Wuhan, Hubei 430062, China

Perovskites

Perovskites General Formula : $A^{2+}B^{4+}X^{2-}{}_3$

Ideal Cubic Perovskite t=1

Distorted Perovskites t<1

Goldschmidt's tolerance factor

$$t=\frac{(r_A+r_O)}{\sqrt{2}(r_B+r_O)}$$

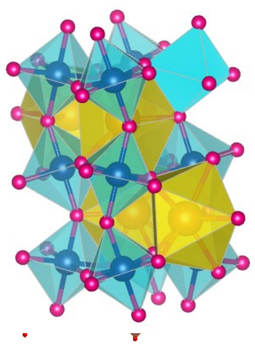

Oxygen Octahedra

Octahedral site B cation

Site A cation

- A is the larger cation, B is the smaller cation
- X is the generally Oxygen or Halogen Material.
- Each corner is shared by BO_6 octahedral with 12 coordinated A cation
- Each A site cations are occupied at the corners of the cube , B cations sit a the body centered sites and Oxygen at the face centered positions.

Super-lattices

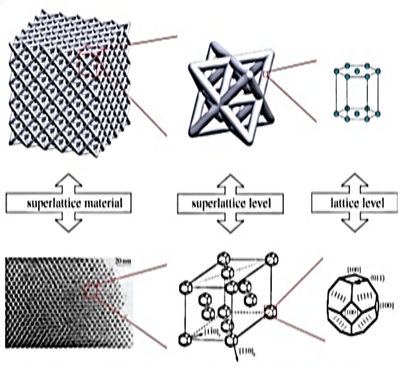

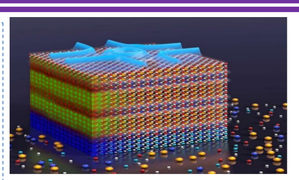

$LaNiO_3$ Thickness 3 nm

$La_{0.7}Sr_{0.3}MnO_3$ Thickness 1.8 nm

$SrTiO_3$ (001) Single crystal substrate

∧ (Super-period)

$LaNiO_3$ Thickness 2.6 nm

$La_{0.7}Sr_{0.3}MnO_3$ Thickness 4.2 nm

$SrTiO_3$ (011) Single crystal substrate

Periodic structure of two or more layers with thickness of each layer typically around several nano-meters.

Applications of Perovskite Super-lattice

- Surface-enhanced Raman spectroscopy based sensors, memory storage, and electronic and optical nanodevices.
- Optoelectronic devices such as solar cells and light emitting diodes.
- Capacitor dielectric for advanced packaging applications
- spintronic and Ferro electromagnets
- Tunable oscillators, as well as tunable filters for wireless applications at cellular, PCS.

Schematic Diagram of PLD

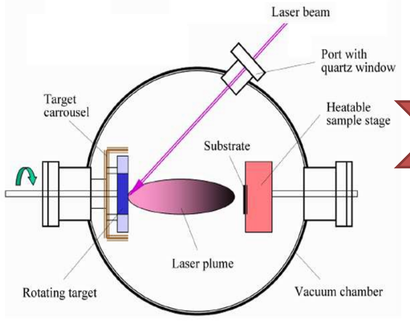

Thin films are prepared by the ablation of one or more targets illuminated by a focused pulsed laser beam.

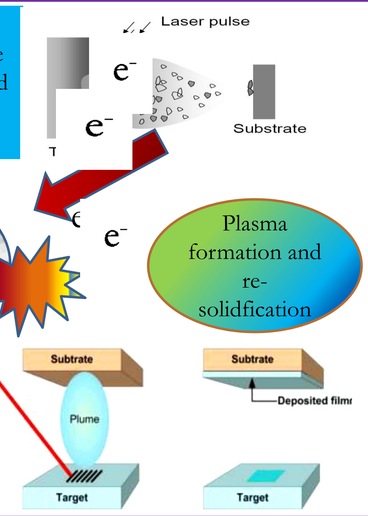

System	Mode 1 (ν_1)	Mode 2 (ν_2)	Mode 3 (ν_3)	Mode 4 (ν_4)	Mode 5 (ν_5)	Mode 6 (ν_6)	Mode 7 (ν_7)	Mode 8 (ν_8)
	A_{1g}	$A_g(2) \rightarrow A_g(7)$	A_g (4)	B_{3g}	E_g Or A_g / B_{2g}	B_{2g}	-	-
SL-001	121.2-129.4	250	284.2	307.5-351.9	397	619.4	688.1	723.7
SL-011	113.5-125.1	253.8	284	325.1-347.4	395.5	619.4	680.3	723.7
SL-111	120.9-136.4	251	288.4	319.7-353.2	394.5	620.2	678.2	730.2

Acknowledgement

For Magnetic Properties:
- DST-FIST Grants SR/FST/PSII-020/2009 and
- SR/FST/PSII-037/2016

For AFM:
- Central instrument facility (CIF) IIT -Guwahati

For Other Measurements:
- Central instrument facility (CIF) , IIT Guwahati

Results

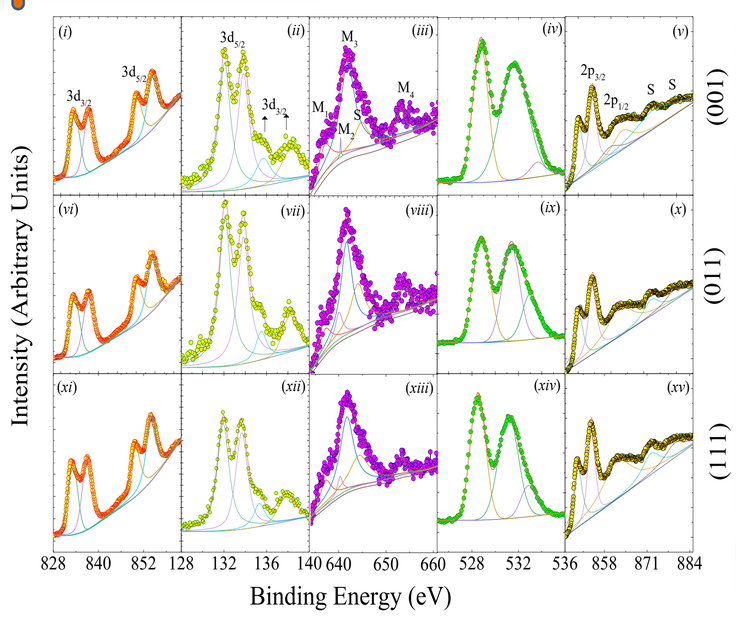

The core level XPS spectra of the respective cations

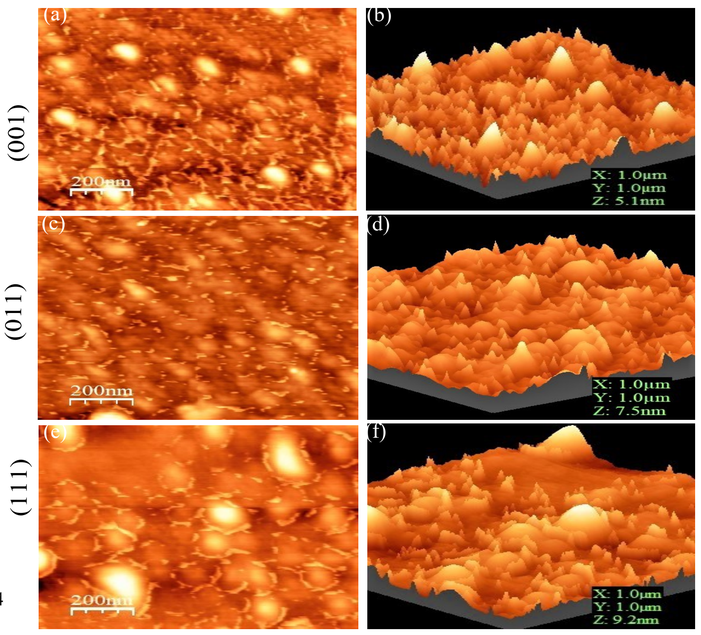

Morphological study by AFM of SL LSMO/LNO (001) , (011) and (111) .

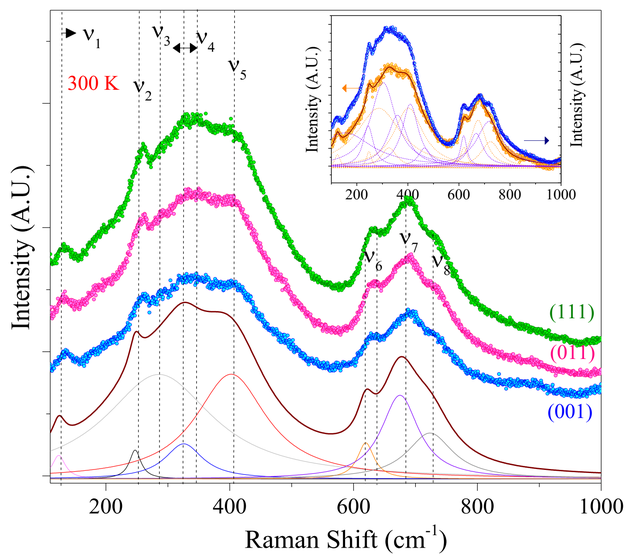

The Raman characteristics of the three SLs and inset depicts the comparison of SL-011 with respect to the bare substatretae of STO-011.

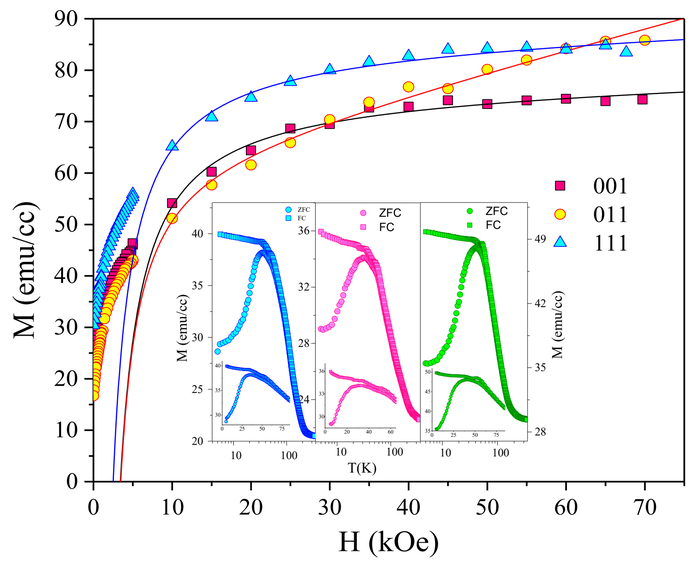

The LAS fit of the three SLs and inset shows the MT chrectersics of the same.

Conclusions

Stranski–Krastanov growth is predominant in the SL-011 oriented superlattice while the other two different crystalline orientations (SL-111 and SL-001) follows the columnar grain growth features.

The presence of mixed valence states of Ni in LNO layers and Mn in LSMO layer and confirms that the charge transferable interfaces are present across the layers.

The entire superlattice systems exhibits ferromagnetic ordering temperatures ($67 \leq T_C \leq 110K$) with altered ground state spin configuration from S = 3/2 due to which an increment in the effective exchange interaction J_{eff} was noticed in these superlattices as compared to the pristine systems LSMO/LNO.

The SL-011 system exhibits bulk anisotropy field $H_K \sim 18$ kOe and cubic anisotropy constant $K_1 \sim 9.3\times10^3$ J/m^3 in comparison to the other two orientations

The Raman spectroscopy data demonstrates the dominant directional dependent features in the investigated system, Overall it is quite evident that all the modes closely resemble the substrate characteristics influencing much of the growth pattern and pointing towards the highly oriented epitaxial growth except the v4 and v8 modes which slightly differ in case of SL-111 superlattices.

References

1) S. Das, … and S. Thota, *J. Phys. D: Appl. Phys*. **51,** 325001 (2018).

2) M. Granada,… and L. B. Steren, *Appl. Phys. Lett.* **91**, 072110 (2007).

3) G. Zhou,.. and X. Xu, *J. Mater. Chem. C* **6**, 582 (2018).

4) M. Gibert, ….and J. M. Triscone, *Nat. Mater*. **11**, 195 (2012).

5) P. Liu and X. Ning, *Phys. B: Condens. Matter* **589,** 412199 (2020).

6) H. Guo,…. and A. C. Komarek, *Nat. Commun*. **9**, 43 (2018).

7) K. Steenbeck and R. Hiergeist, *Appl. Phys. Lett.* **75**, 12 (1999).

8) J. M. D. Coey,…. and L. Ranno, *Phys. Rev. Lett.*, **75**, 21 (1995).

9) B. C. Behera,… and W. Prellier, *Appl. Phys. Lett.* **104**, 092406 (2014).

Pulsed Laser Growth of $[Pr_{1-x}Ca_xMnO_3/SrTiO_3]_{15}$ Superlattices

Ravi Kiran Dokala[1], Shaona Das[1], S Ghosh[1], Sujit Das[2] and S. Thota[1]

[1] *Department of Physics, Indian Institute of Technology Guwahati-781039, Assam, India*

[2] *Department of Material science and Engineering, University of California, Berkeley, California, United States of America*

Perovskites

Perovskites
General Formula : ABO_3

Ideal Cubic Perovskite t = 1

Distorted Perovskite t < 1

$$t = \frac{r_A + r_O}{\sqrt{2}\,(r_B + r_O)}$$

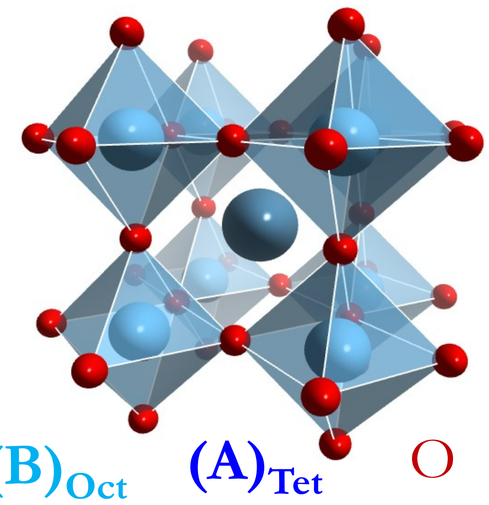

Superlattices

- Super-lattices: Periodic structure of two or more layers with thickness of each layer around several nano-meters.
- Referred to lower dimensional structures like array of quantum Wells

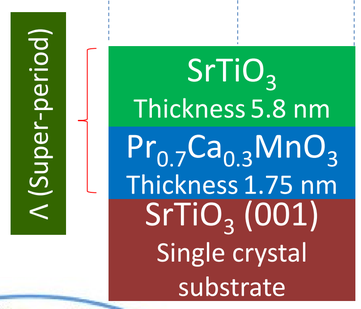

Applications

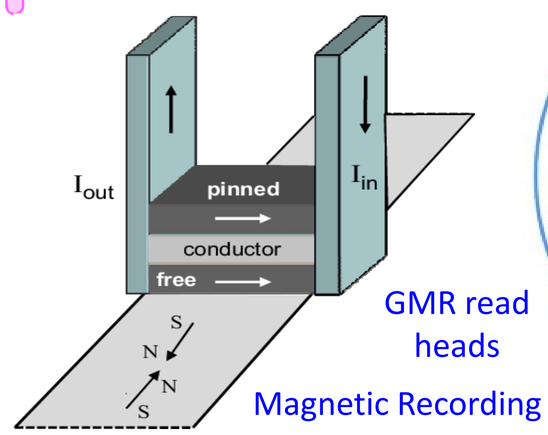

GMR read heads

Magnetic Recording

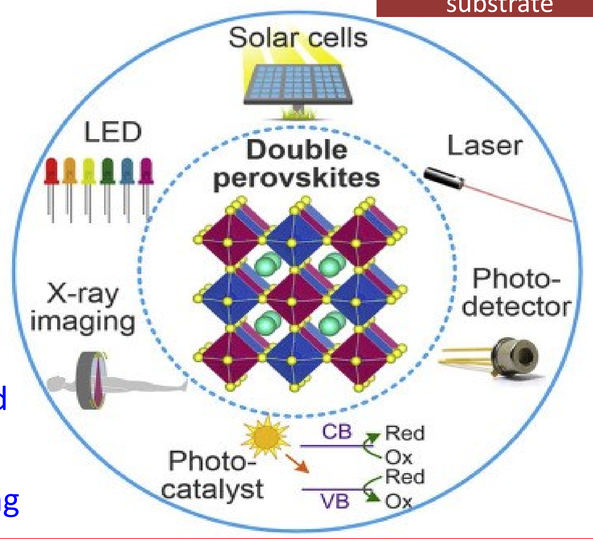

Fabrication Details

Pulsed Laser Ablation (PLD)

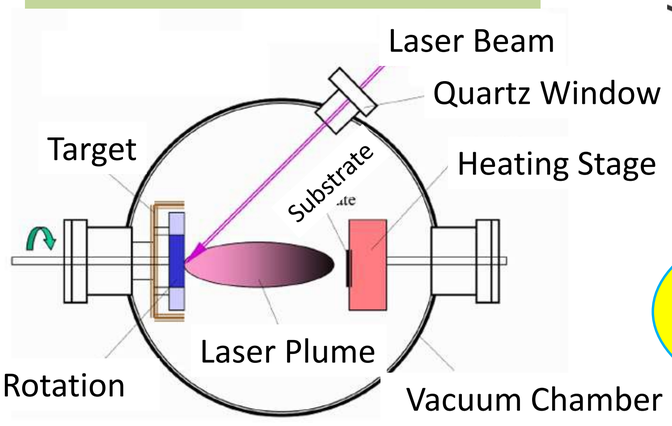

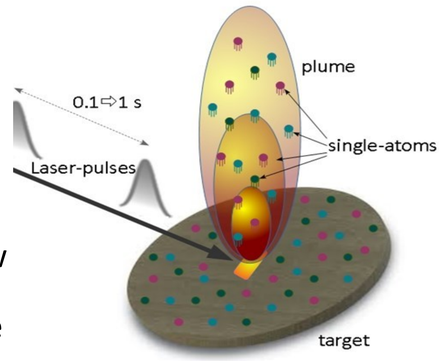

Plasma formation & re-solidfication

Results & Discussion

Superlattice/Substrate	M_S (*emu/cc*)	K_1 (× 10^4 *erg/cc*)	H_K (× 10^3 *Oe*)
$[Pr_{0.7}Ca_{0.3}MnO_3/SrTiO_3]_{15}/SrTiO_3$	181	80	9.0
$[Pr_{0.7}Ca_{0.3}MnO_3/SrTiO_3]_{15}/LaAlO_3$	386	5.77	0.31
$[Pr_{0.5}Ca_{0.5}MnO_3/SrTiO_3]_{15}/SrTiO_3$	69	1.42	0.38
$[Pr_{0.5}Ca_{0.5}MnO_3/SrTiO_3]_{15}/LaAlO_3$	123	1.77	0.33

Saturation magnetisation(M_S); Magnetic anisotropy constant(K_1); Anisotropy field (H_K)

Acknowledgement:

DST-FIST SR/FST/PSII-020/2009 and SR/FST/PSII-037/2016.
Central Instrument Facility, IITG. CSIR Funding for JRF, Govt. of India.

Crystal Structure

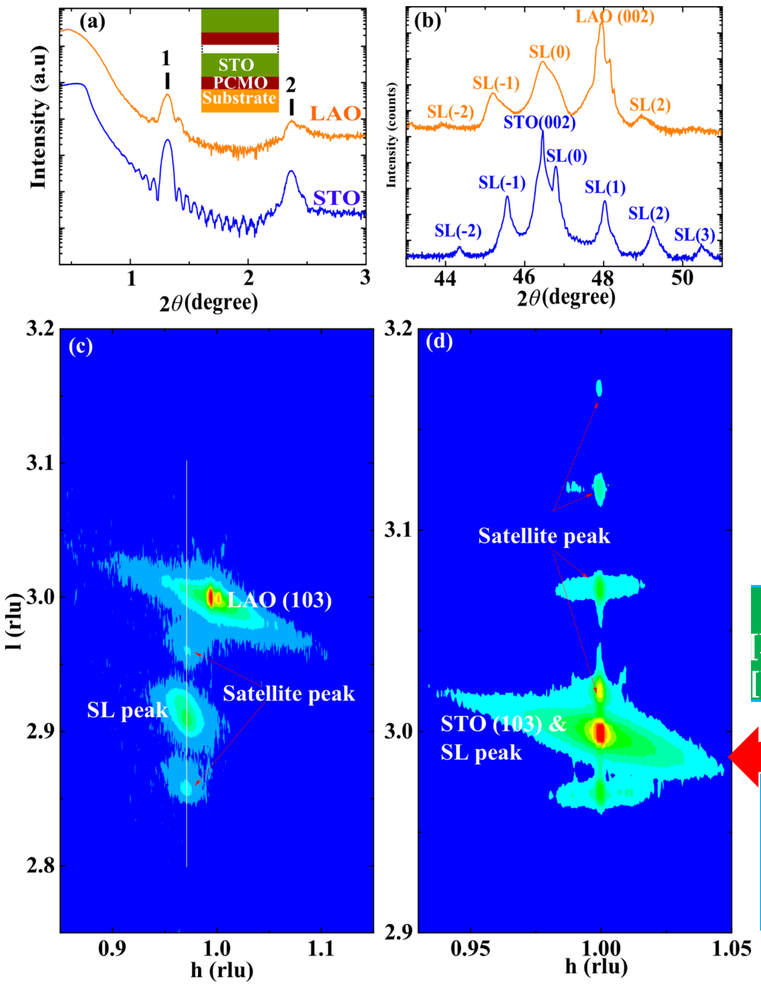

XRR of the SLS on STO(001) & LAO(001), and
Reciprocal Space Mapping of SLs around the (103) reflection.

Atomic Force Microscopy

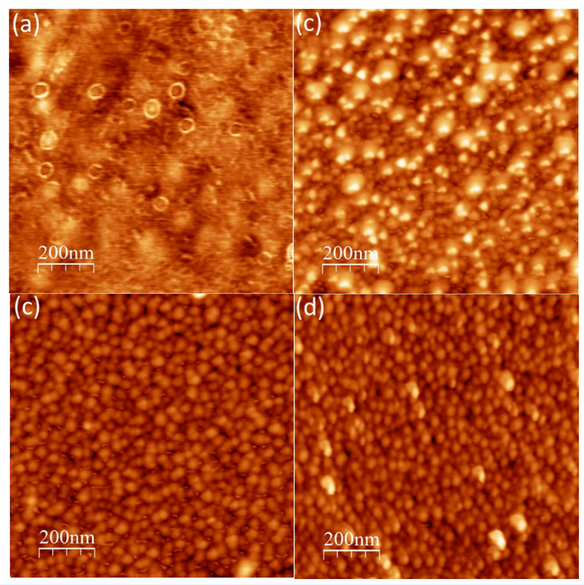

Surface Morphology study by AFM
$[Pr_{70}Ca_{30}MO/STO]_{15}$ on STO(001) & LAO(001)
$[Pr_{50}Ca_{50}MO/STO]_{15}$ on STO(001) & LAO(001)

Raman spectra

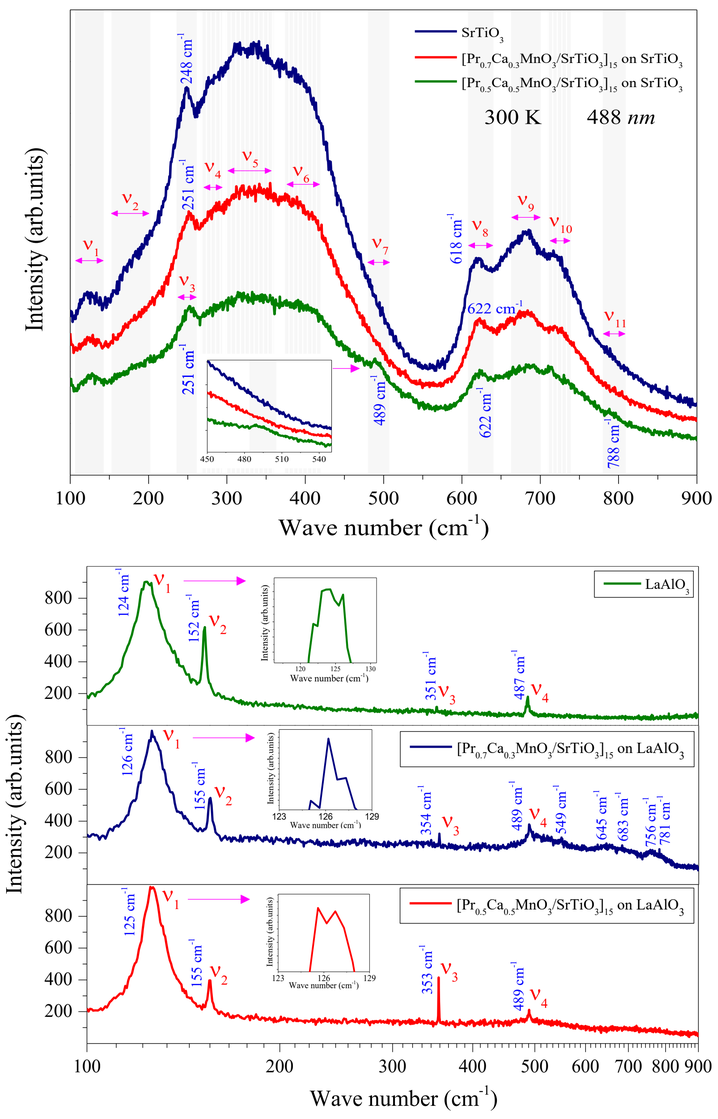

Magnetic Properties

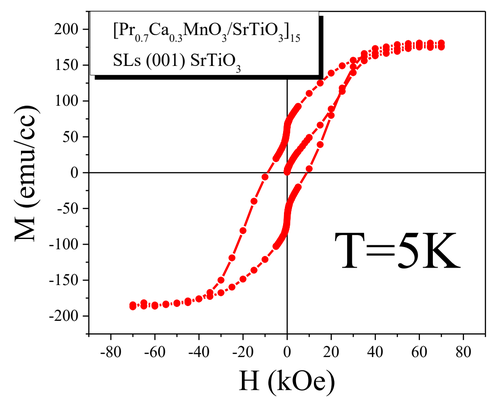

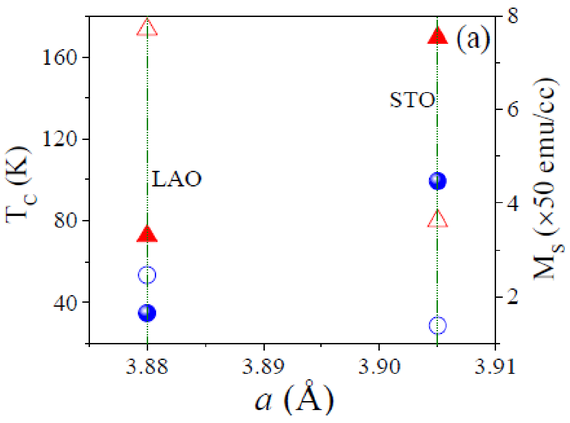

On $LaAlO_3$

Mode ν_4 (*489 cm^{-1}*) –Effect of **Praseodymium (Pr)**
$A_g(1) \rightarrow A_g(3)$
O_2 anti-stretching → MnO_6 bending
Basic distortion of JT from [010] → [101]

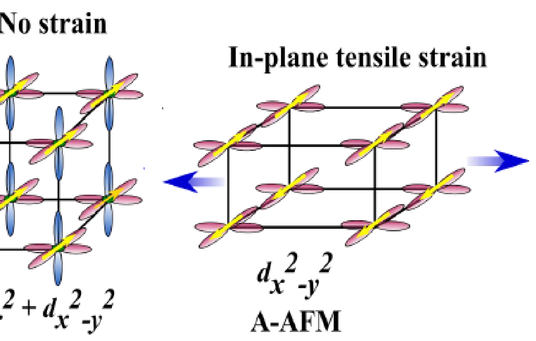

Mode ν_7 (489 *cm^{-1}*) - Two small spikes

On $SrTiO_3$

$B_{2g}(3)$
out-of-phase MnO_6 bending
basic distortion of [101]

Ag(1) → Ag(3)
Due to O_2 anti-stretching → MnO_6 bending
basic JT distortion from [010] → [101].

References:

R. von Helmolt, J. Wecker, B. Holzapfel, and K. Samwer, "Giant negative magnetoresistance in perovskitelike La2/3Ba1/3MnO_x ferromagnetic films," Phys. Rev. Lett. 71, 2331 (1993).
S. Thota, K. Roychowdhury, V. Thakare, S. Ganguli, Z. Chen, and S. Das, "Structural and magnetic properties of $La_{0.7}Sr_{0.3}MnO_3/LaCoO_3$ heterostructures," Appl. Phys. Lett. 113, 122405 (2018).

Exotic self-trapped superstructures in spin-orbit coupled spin-2 condensate

Pardeep Kaur[a]*, Sandeep Gautam[a], and S. K. Adhikari[b]

[a]*Department of Physics, Indian Institute of Technology Ropar, Rupnagar 140001, Punjab, India*

[b]*Instituto de Física Teórica, Universidade Estadual Paulista - UNESP, 01.140-070, São Paulo, Brazil*

[*]*Email: 2018phz0004@iitrpr.ac.in*

Introduction

Spinor Bose Einstein Condensates (BECs)

- An ultracold atomic gas in optical traps having spin-f per atom led to experimental realization of 2f+1 component BECs known as Spinor BECs. [1]
- In mean-field approximation, spin-2 BEC is described by set of five coupled time-dependent nonlinear partial differential equations with 1st order derivative in time and 2nd order derivative in space known as **coupled Gross-Pitaevskii equations**. (CGPEs)
- Spin-2 condensates can have three ground state phases depending on relative strength of spin-dependent interaction terms i.e. c_0, c_1, and c_2.

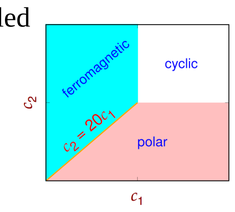

Spin-Orbit Coupling (SOC)

- SOC is the coupling between motion of entire atom to its hyperfine spin.
- SOC can be engineered in these neutral spinor BECs by controlling the atom light interaction leading to generation of artificial gauge potentials coupled to the atoms.[2]
- Interplay of SOC and the mean-field interactions give rise to a variety of ground states.[3]
- SO-coupling leads to the stabilization of self-trapped solutions like bright solitons.
- **Bright Soliton** is a self-bound multi-component solitary wave which maintains its shape while moving with a constant velocity.[4]
- Another recent development in the field is the experimental realization of supersolid like stripe phase in SO-coupled pseudospin-1/2 spinor condensates.[5]
- **Supersolid like phase** corresponds to the simultaneous (and spontaneous) breaking of continuous translational and global gauge symmetries and posses both diagonal and off-diagonal order.
- The **objective** of this work is to construct quasi-two-dimensional (q2D) self-trapped stable structures in SO-coupled spin-2 condensate.

Method

- Condensate is considered free along the x-y plane and is confined by a harmonic trap along the z-direction.
- The **Rashba SO-coupling** considered is $H_{SO} = \gamma\,(p_y S_x - p_x S_y)$
- At zero temperature, under mean-field approximation, the five CGPEs in the presence of Rashba SOC for the wave-function components ϕ_j are given in dimensionless form as

$$i\frac{\partial\phi_{\pm2}}{\partial t} = \mathcal{H}\phi_{\pm2} + c_0\rho\phi_{\pm2} + c_1\{F_{\mp}\phi_{\pm1} \pm 2F_z\phi_{\pm2}\} + c_2\frac{\Theta\phi^*_{\mp2}}{\sqrt{5}} + \Gamma_{\pm2}$$

$$i\frac{\partial\phi_{\pm1}}{\partial t} = \mathcal{H}\phi_{\pm1} + c_0\rho\phi_{\pm1} + c_1\left\{\sqrt{\frac{3}{2}}F_{\mp}\phi_0 + F_{\pm}\phi_{\pm2} \pm F_z\phi_{\pm1}\right\} - c_2\frac{\Theta\phi^*_{\mp1}}{\sqrt{5}} + \Gamma_{\pm1}$$

$$i\frac{\partial\phi_0}{\partial t} = \mathcal{H}\phi_0 + c_0\rho\phi_0 + c_1\sqrt{\frac{3}{2}}\{F_-\phi_{-1} + F_+\phi_1\} + c_2\frac{\Theta\phi^*_0}{\sqrt{5}} + \Gamma_0$$

- where $\mathcal{H} = -\frac{1}{2}\left(\frac{\partial^2}{\partial x^2} + \frac{\partial^2}{\partial y^2}\right)$, $\rho = \sum_{j=-2}^{2}|\phi_j|^2$, $\Theta = \frac{2\,\phi_2\,\phi_{-2} - 2\phi_1\,\phi_{-1} + \phi_0^2}{\sqrt{5}}$,
- $F_z = \sum_{j=-2}^{2} j|\phi_j|^2$, $F_- = F_+^* = 2\,\phi^*_{-2}\phi_{-1} + \sqrt{6}\,\phi^*_{-1}\phi_0 + \sqrt{6}\,\phi^*_0\phi_1 + 2\phi_2\phi_1^*$; $F_{\pm} = F_x \pm F_y$
- Θ is the spin-singlet pair amplitude. ρ is the total density. F_x, F_y, and F_z are 3 components of spin-density vector **F**.
- The interaction parameters are given as

$$c_0 = \frac{2\sqrt{2}\pi N(4a_2+3a_4)}{7a_{osc}};\quad c_1 = \frac{2\sqrt{2}\pi N(a_4-a_2)}{7a_{osc}};\quad c_2 = \frac{2\sqrt{2}\pi N(7a_0-10a_2+3a_4)}{7a_{osc}};$$

- a_0, a_2, and a_4 are s-wave scattering lengths in 3 allowed scattering length channels for spin-2 BEC.
- The SO-coupling terms are given as $\Gamma_{\pm2} = -i\gamma\left(\frac{\partial\phi_{\pm1}}{\partial y} \pm i\frac{\partial\phi_{\pm1}}{\partial x}\right)$
- $\Gamma_{\pm1} = -i\sqrt{\frac{3}{2}}\gamma\left(\frac{\partial\phi_0}{\partial y} \pm i\frac{\partial\phi_0}{\partial x}\right) - i\gamma\left(\frac{\partial\phi_{\pm2}}{\partial y} \mp i\frac{\partial\phi_{\pm2}}{\partial x}\right)$; $\Gamma_0 = -i\sqrt{\frac{3}{2}}\gamma\left(\frac{\partial\phi_1}{\partial y} + \frac{\partial\phi_{-1}}{\partial y} - i\frac{\partial\phi_1}{\partial x} + i\frac{\partial\phi_{-1}}{\partial x}\right)$
- To obtain the stationary states, we have solved these CGPEs with **Fourier Spectral method**.
- The dynamic stability of these solutions is confirmed by real-time evolution.

Results

(a) Phase Requirement

- The permitted vortex configuration in a spinor BEC depend on the inter-component phase relationships.
- The interaction and the energy contribution from the SO-coupling leading to following independent relationships among permitted winding numbers :
  $w_2 - w_1 + 1 = 0$; $w_1 - w_0 + 1 = 0$; $w_{-2} - w_{-1} - 1 = 0$; $w_1 - w_0 + 1 = 0$;
- The allowed winding number combinations are (-2, -1, 0, 1, 2), (-1, 0, 1, 2, 3), (0, 1, 2, 3, 4) and higher.

(b) Single Particle Hamiltonian

- One eigen function of the single-particle Hamiltonian with (minimum) energy $-2\gamma^2$ is
  $\Phi = \frac{e^{i\,\boldsymbol{k}.\boldsymbol{r}}}{4}\left(e^{-2i\varphi} \;\; -2e^{-i\varphi} \;\; \sqrt{6} \;\; -2e^{-i\varphi} \;\; e^{2i\varphi}\right)^T \equiv \zeta(\varphi)\,e^{i\,\boldsymbol{k}.\boldsymbol{r}}$ where $\varphi = tan^{-1}\left(\frac{k_y}{k_x}\right)$ and $k^2 = k_x^2 + k_y^2 = (2\gamma)^2$
- The superposition of two counter-propagating plane waves represents a stripe phase (S)
  $\Phi_S = \frac{1}{\sqrt{2}}\left[\zeta(0)e^{2i\gamma\,x} + \zeta(\pi)e^{-2i\gamma\,x}\right]$
- The superposition of three plane waves whose propagation vectors make an angle $2\pi/3$ with each other gives a triangular superlattice (TS)
  $\Phi_{TL} = \frac{1}{\sqrt{3}}\left[\zeta(0)e^{2i\gamma\,x} + \zeta(2\pi/3)e^{i\gamma(-x+\sqrt{3}y)} + \zeta(4\pi/3)e^{i\gamma(-x-\sqrt{3}y)}\right]$
- The superposition of four plane waves whose propagation vectors make an angle $\pi/2$ with each other gives a square superlattice (SS)
  $\Phi_{SS} = \frac{1}{2}\left[\zeta(0)e^{2i\gamma x} + \zeta(\pi/2)e^{i2\gamma y} + \zeta(\pi)e^{-2i\gamma x} + \zeta(3\pi/2)e^{-i2\gamma y}\right]$
- The most general solution is by considering the superpositions of eigenfunctions with k pointing along all directions in 2D plane gives rise to Multi-ring (MR) soliton.

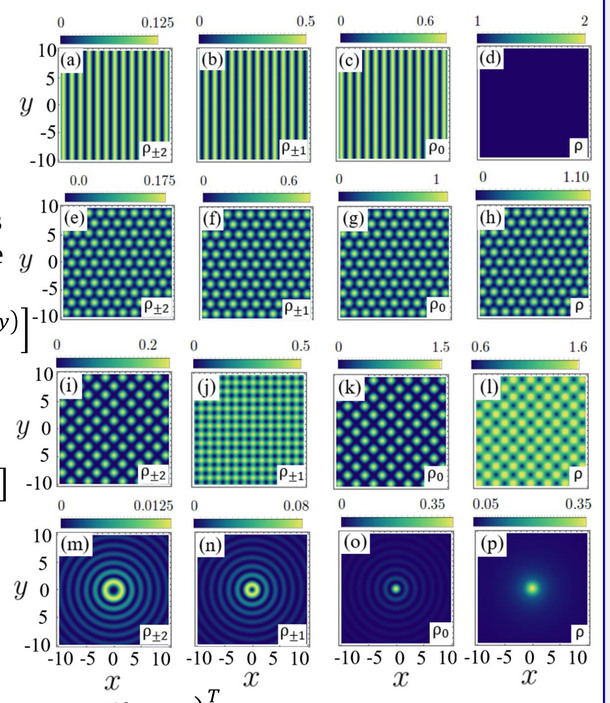

- $\Phi_{MR} = \left(-e^{-2i\theta}J_2(p) \;\; -2ie^{-i\theta}J_1(p) \;\; \sqrt{6}J_0(p) \;\; -2ie^{-i\theta}J_1(p) \;\; -e^{-2i\theta}J_2(p)\right)^T$; $p = 2\gamma r$

The component densities and corresponding total density for these degenerate solutions corresponding to $|\Phi_S|^2$, $|\Phi_{TS}|^2$, $|\Phi_{SS}|^2$ and $|\Phi_{MR}|^2$ are shown in 1st, 2nd, 3rd and 4th row, respectively.

(c) Numerical Results

- The ground state for small SO-coupling strength is radially *symmetric vortex-bright(-ring)* soliton (-2,-1,0,1,2) for cyclic, polar and weakly ferromagnetic interactions e.g. for ferromagnetic phase having c_0= -2.5, c_1= -0.025, $c_2 = 0.25$, $\gamma = 0.5$ is shown at the right.

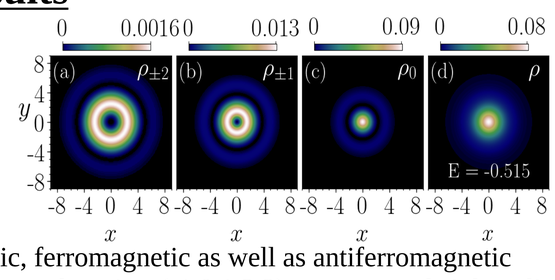

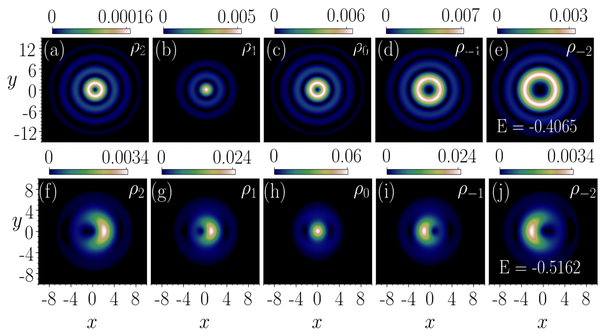

- For intermediate SO-coupling strengths, *triangular self-trapped superlattice* appears as a quasi-degenerate state in addition to the vortex-bright soliton of type (-2,-1,0,1,2) type soliton. e.g. with c_0= -2.5, c_1= -0.1, $c_2 = 0.25$, $\gamma = 0.5$ is shown at the right.

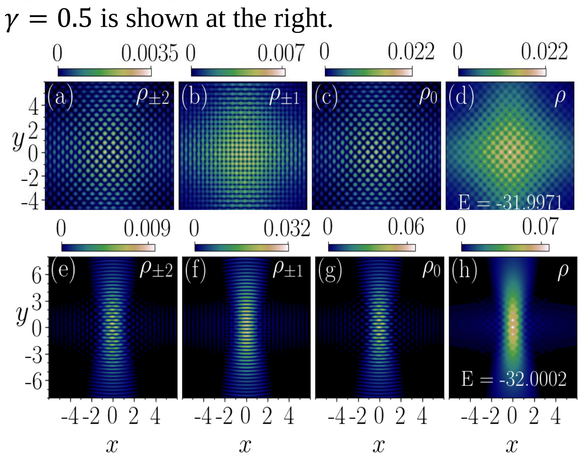

- For cyclic, ferromagnetic as well as antiferromagnetic interactions, there is a (-1,0,1,2,3) type *vortex bright soliton* that exists as a metastable state. e.g. for ferromagnetic phase having c_0= -2.5, c_1= -0.025, $c_2 = 0.25$, $\gamma = 0.5$ is shown at the left in 1st row.
- For sufficiently strong ferromagnetic interactions, *asymmetric vortex bright* solitons emerges as the ground state e.g. with c_0= -2.5, c_1= -0.1, $c_2 = 0.25$, $\gamma = 0.5$ is shown at the left in 2nd row.

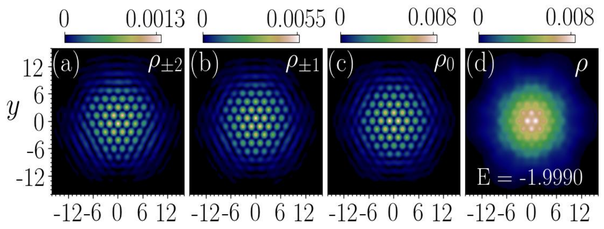

- For sufficiently strong SOC strengths, for case of ferromagnetic interactions, we get five types of quasi-degenerate states as following (1) *self-trapped square-superlattice*, (2) *vortex-bright (-ring) soliton*, (3) *asymmetric bright soliton*, (4) a *stripe soliton*, and (5) *super-stripe lattice*.
- For cyclic, and antiferromagnetic interactions, we get four of the aforementioned degenerate states except the asymmetric bright soliton.
- In polar phase, two of these *square super-lattice* (1st row in left) and *super-stripe lattice* (2nd row at left) for $c_0 = -0.15$, $c_1 = 0.25$, $c_2 = -1$ and $\gamma = 4$ are shown.

Conclusions

- ✓ Studied the self-trapped stationary state solutions of the SO-coupled spin-2 BEC.
- ✓ Established the permissible winding number relationships for the system by minimizing the energy contributions from spin-dependent interactions and SO-coupling.
- ✓ The degenerate ground state solutions of the non-interacting SO-coupled condensate are discussed.
- ✓ At small SO-strengths, *bright ring solitons* appear across the three phases as stationary state solution.
- ✓ At moderate to strong SO-coupling strengths ; emergence of multiple quasi degenerate self-trapped solutions is discussed e.g. *the hexagonal-super lattice, super-square lattice*, and *superstripe square lattice* solutions.
- ✓ The stability of these solutions is checked via real-time propagation.

References

1). Y. Kawaguchi and M. Ueda, Phys. Rep. 520, 253 (2012)
2). Y.-J. Lin, K. Jimenez-Garcia, and I.B. Spielman, Nature 471, 83 (2011)
3). Y. Li, L. P. Pitaevskii, and S. Stringari, Phys. Rev. Lett.108, 225301 (2012).
4). Y. V. Kartashov, G. E. Astrakharchik, B. A. Malomed,and L. Torner, Nature Rev. Phys.1, 185 (2019).
5). J.-R. Li, J. Lee, W. Huang, S. Burchesky, B. Shteynas, F.Ç. Top, A. O. Jamison, and W. Ketterle, Nature 543, 91 (2017)